Università degli Studi di Padova

Dipartimento di Fisica e Astronomia "Galileo Galilei"

Tesi di Laurea Magistrale in Fisica

Reconstructing the primordial power spectrum: implications for cosmological models

Relatore:
Prof. Nicola Bartolo
Correlatori:
Dott. Michele Liguori
Prof. Licia Verde

Laureando: Andrea Ravenni
Matricola: 1084470

Anno Accademico 2014/2015

Contents

Chapter 1

Introduction

Cosmology is now a precision science. In the last decade satellites and telescopes collected a huge amount of data. The experiments that are now under development will provide us with even more precious information. In the next few years the analysis of all those information will greatly improve our understanding of the Universe history. The parts we can hope will be clarified the most are those that are now the most obscure: the furthest moments in the past, and the nearest to us. The Hot Big Bang model works really fine, but what was before — inflation – and what is at the end of it — structures growth and accelerated expansion — still puzzles the scientific community.

If we look at the Universe on scales big enough it surely appears homogeneous and isotropic. It is really straightforward to describe the evolution of a universe with those characteristics. Cosmologists found out that a homogeneous universe filled with roughly one third of cold dark matter and two third of some kind of energy with negative pressure, plus smaller quantities of baryons and radiation, fits experimental data astonishingly well.

But such a description surely misses the main point. The Universe does not stop to homogeneity. Just by looking at the sky one can see that it is full of structure, but the same applies to scales that cannot be seen by bare eyes as well. To give a description somewhat satisfying it is necessary to add perturbations. Luckily enough those are so small, that most of the time working at linear order is more than acceptable. Although small, perturbations are the important piece of the puzzle.

Inflation has been firstly introduced to solve the three main problems of the Hot Big Bang model, the flatness, the horizon, and the monopole problems, but people started being interested in it because it predicts the first density perturbations in the primordial Universe. In chapter 2 we will review the inflation dynamics and explain how quantum fluctuations of the field driving inflation, the inflaton, could have been stretched to cosmological scales. Those fluctuations were the seeds for the Cosmic Microwave Background (CMB) temperature
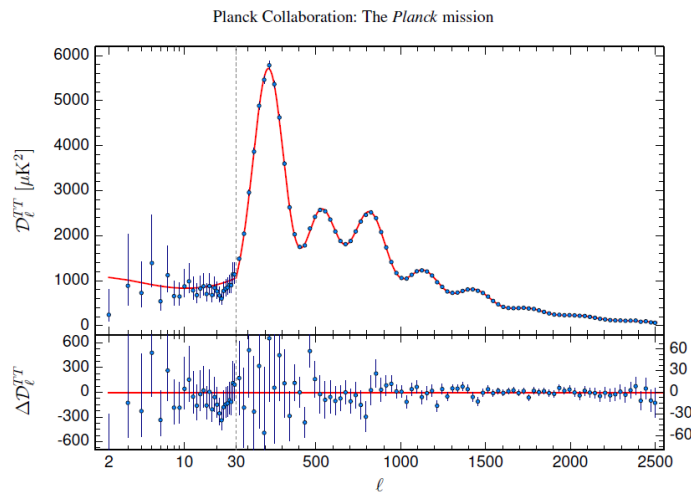
Figure 1.1: The *Planck* 2015 temperature power spectrum. The best fit base ΛCDM theoretical spectrum fitted to the *Planck* TT + lowP likelihood is plotted in the upper panel. Residuals with respect to this model are shown in the lower panel. The error bars show $\pm 1\sigma$ uncertainties. Figure from [1].

anisotropies and for structure growth, that eventually produced the Large–Scale Structure (LSS) in the distribution of galaxies and the underlying dark matter that we observe today.

The basic model that incorporates all those features is the ΛCDM model, i.e. a Universe filled (mainly) with cosmological constant and cold dark matter. It relies on surprisingly few free parameters, just six, but predicts large scale behaviours of our Universe to a very high degree of accuracy. How to parametrize the six degrees of freedom is somewhat arbitrary. A convenient choice is to use the Hubble parameter evaluated today H_0, the optical depth to reionization τ, the baryon density today Ω_b, the cold dark matter density today Ω_{cdm}, the amplitude of the primordial curvature perturbations at a pivot scale $k_0 = 0.02$ Mpc$^-$1 A_s, and finally the power law index of the perturbations spectrum n_s. We will talk in more detail of the cosmological parameters, and how they are measured in section 5.2.1.

The most precise checks of the ΛCDM model come from measurements of CMB temperature (in figure 1.1) and polarization (in figure 1.2) anisotropies made by the *Planck* satellite [1].

The best fit values of the ΛCDM model are shown in table 1.1.

In the past a general lack of data promoted the birth of plenty of different models, all in perfect agreement with the few available observations. Current day experiments (such as WMAP [2], SDSS [3], and many others), led by *Planck*, are excluding almost all of them. Only small deviations from the ΛCDM model are allowed, but still there are multiple models with those characteristics. The aim
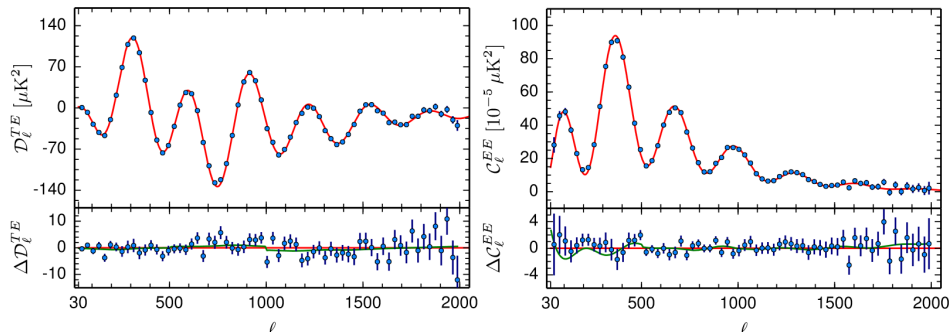
Figure 1.2: Frequency-averaged TE (left) and EE (right) spectra. The theoretical TE and EE spectra plotted in the upper panel of each plot are computed from the best fit model of fig. 1.2. Residuals with respect to this theoretical model are shown in the lower panel in each plot. The error bars show $\pm 1\sigma$ uncertainties. Figure from [1].

Parameter	Definition	*Planck* TT,TE,EE + Low P
$\Omega_b h^2$	Baryon density today	0.02225 ± 0.00016
$\Omega_{cdm} h^2$	Cold dark matter density today	0.1198 ± 0.0015
τ	Optical depth due to reionization	0.079 ± 0.017
$\ln(10^{10} A_s)$	Log power of the primordial curvature perturbations	3.094 ± 0.034
n_s	Scalar spectrum power-law index ($k_0 = 0.05 \mathrm{Mpc}^{-1}$)	0.9645 ± 0.0049
H_0	Current Hubble parameter in km s^{-1}Mpc^{-1}	67.27 ± 0.66

Table 1.1: Parameters of the base ΛCDM cosmology computed from the 2015 baseline *Planck* likelihoods. Table from [1].

of the present work is to reconstruct the shape of the primordial power spectrum (we will define it precisely in chapter 2, it describes primordial density fluctuations), and its deviations from the power-law assumed in the ΛCDM model. Since different inflation models, discussed in chapter 3, predict different power spectra, a constraint on the shape could exclude some of them.

In chapter 4 we describe the methodology of our reconstruction. As it is a minimally parametric reconstruction it has the advantages of being model independent. It does not require an input such as a reference shape with parameters to fit, that could easily be wrong. This allows to give more freedom to data: we can check what model data support and not only if a specific model is supported by data. A parametric analysis in fact would need to be repeated for every possible theoretically justified shape, to determine which one is the most likely. On the other hand, minimally parametric analysis means that we will get a definite shape with which we can easily distinguish competing classes of models. Moreover, the reconstructed shape could even be of a kind not considered by any model. That would be a signal of new physics that would require fresh ideas and new theories

that can support it. Of course there are downsides in this method, the main of which is that errors are likely to be greater than in a parametric reconstruction.

In chapter 5 we explain how the methods introduced in the previous chapter are implemented in our case. Moreover we investigate the implication of our work on a very discussed topic: cosmological evidence of neutrino masses. Since many studies, combining different datasets reach opposite conclusions on the basis of what signal they focus on, we hope that our analysis, being minimally parametric could help solve the question. Furthermore we point out that a reconstruction of the primordial power spectrum that performs a joint analysis of both *Planck* CMB power spectrum and matter power spectrum is still missing in the literature. Our work fills this lacuna.

In chapter 6 we present the results of our analysis and finally in chapter 7 we draw our conclusions.

Chapter 2

Inflation and primordial power spectrum

Inflation is the most widely accepted scenario that solves the main problems of the Hot Big Bang model (HBB) [4]. Those are the flatness problem, the horizon problem and the unwanted relics problem. All of them can be solved to some degree by an early phase of accelerated expansion of the Universe. Inflation is exactly this: an epoch of accelerated expansion that is thought to have occurred before the times described by the HBB. In this chapter we do not present exhaustively the inflation (see [4] for a didactic introduction or [5] for a more advanced review). Instead we tried to follow the straightest path that leads from inflation to the main topic of this thesis, the primordial power spectrum.

The fundamental equations we will need are the Einstein equations. They link the metric, through the Riemann tensor, to the Universe energy-momentum tensor $T_{\mu\nu}$

$$R_{\mu\nu} - \frac{1}{2}Rg_{\mu\nu} = 8\pi G T_{\mu\nu}, \tag{2.1}$$

where $R_{\mu\nu}$ and R are respectively the Ricci tensor and scalar and G is the universal gravitational constant.

For an homogeneous and isotropic universe the metric is the Robertson-Walker (RW) [4]. If we choose the signature $(-,+,+,+)$ it is

$$ds^2 = -dt^2 + a(t)^2 \left[\frac{dr^2}{1 - kr^2} + r^2(\sin^2\theta d\phi^2 + d\theta^2) \right]. \tag{2.2}$$

The curvature is controlled by k. For $k = 0$ we have a flat universe, for $k = +1$ a close universe and for $k = -1$ an hyperbolic universe. The parameter $a(t)$ is known as the scale factor, and it parametrizes the expansion of the Universe. It is normalized so that today its value is 1.

The set of equations that describe the evolution of such a universe are the

9

Friedmann equations. Choosing the energy-momentum tensor of a perfect fluid

$$T^{\mu\nu} = (\rho + p)u^\mu u^\nu + pg^{\mu\nu} \tag{2.3}$$

in the Einstein equations we obtain the three Friedmann equations, two of which are independent:

$$H^2 \equiv \frac{\dot{a}^2}{a^2} = \frac{8\pi G}{3}\rho - \frac{k}{a^2}, \tag{2.4}$$

$$\ddot{a} = -\frac{4\pi G}{3}\ a\ (\rho + 3p), \tag{2.5}$$

$$\dot{\rho} = -3H(\rho + p). \tag{2.6}$$

Notice that we have defined also the Hubble parameter H.

By definition inflation is a period of accelerated expansion, so we should impose that the LHS of Eq. (2.5) is greater than zero

$$0 < \ddot{a} = -\frac{4\pi G}{3}\ a\ (\rho + 3p) \quad \Rightarrow \quad p < -\frac{1}{3}\rho, \tag{2.7}$$

where we used the fact that the scale factor can not be negative. ρ can be interpreted as an energy density, so the most logical thing is to assume that it is a positive quantity. Thus p, which is a pressure field, must be negative during inflation. To be precise it has to be less than -1/3ρ to let expansion accelerate. Inflation has to be generated by something with an energy-momentum tensor fulfilling this requirement.

A possible candidate is a cosmological constant, an additional term on the RHS of Einstein equation such as $-\Lambda g_{\mu\nu}$. If the energy density in the Einstein equations is dominated by a cosmological constant then we obtain

$$p_\Lambda = -\rho_\Lambda = -\frac{\Lambda}{8\pi G}, \tag{2.8}$$

$$H^2 = \frac{\Lambda}{3}, \tag{2.9}$$

which has solution

$$a(t) = a_i e^{\frac{\Lambda}{3}(t-t_i)}. \tag{2.10}$$

This type of expansion, with a scale factor that grows exponentially, is called de Sitter phase.

The modern interpretation, which has roots in particle physics, is that Λ is linked to quantum fluctuations of the vacuum. If we require that the energy momentum tensor vacuum expectation value is Lorentz invariant, due to general covariance we have

$$\langle T_{\mu\nu} \rangle = -\langle\rho\rangle\, g_{\mu\nu}. \tag{2.11}$$

So the vacuum expectation value of the stress energy tensor works exactly like a cosmological constant.

This is a hint that, as we already anticipated, the dynamic of a suitable field may drive the inflation. Since observationally we know our Universe is isotropic, trying to use a scalar field to generate the inflation would be a good guess. We will now study the dynamics of a scalar field in FRW, showing that it has the right properties to be the inflaton.

The Lagrangian of the scalar field φ is

$$\mathcal{L}(\varphi, g) = -\frac{1}{2} D_\mu \varphi D^\mu \varphi - V(\varphi), \tag{2.12}$$

where $g \equiv -\det[g_{\mu\nu}]$, and $V(\Phi)$ is the potential of the scalar field. We point out that we are working in an effective field theory framework, so we will never worry about renormalizability.

The Klein-Gordon equation in FRW is

$$\Box_g \, \varphi = +\frac{\partial V}{\partial \varphi}, \tag{2.13}$$

or explicitly

$$\ddot{\varphi} + 3H\dot{\varphi} - \frac{\nabla^2 \varphi}{a^2} = -\frac{\partial V}{\partial \varphi}. \tag{2.14}$$

We note the presence of the friction term $3H\dot{\varphi}$ due to the Universe expansion.

In general relativity the energy-momentum tensor is defined as

$$T^{\mu\nu} = \frac{-2}{\sqrt{g}} \frac{\delta S}{\delta g_{\mu\nu}}. \tag{2.15}$$

So if we consider a minimal coupling with the metric as in [5], and the fact that covariant derivative and derivative coincide for scalars, the energy-momentum tensor of φ is

$$T_{\mu\nu} = \partial_\mu \varphi \, \partial_\nu \varphi + \mathcal{L}_\varphi g_{\mu\nu}. \tag{2.16}$$

It is convenient to split the scalar field in two contributions: the classical background and the quantum fluctuations

$$\varphi(\mathbf{x}, t) = \varphi_0(t) + \delta\varphi(\mathbf{x}, t). \tag{2.17}$$

The classical background is the v.e.v. of the field

$$\varphi_0(t) \equiv \langle \varphi(\mathbf{x}, t) \rangle. \tag{2.18}$$

Now we will analyse first the evolution of the homogeneous background and then the evolution of the fluctuations. For this homogeneous field the Klein-Gordon equation (2.14) reduces to

$$\ddot{\varphi}_0 + 3H\dot{\varphi}_0 = -V'(\varphi_0). \tag{2.19}$$

It is easy to evaluate the background energy-momentum tensor. Plugging the FRW metric in Eq. (2.16), we obtain for the temporal-temporal and the spatial-spatial entries of the tensor

$$-\rho_{\varphi_0} = T^0_{\ 0} = -\left(\frac{1}{2}\dot{\varphi}_0^{\ 2} + V(\varphi_0)\right), \tag{2.20}$$

$$p_{\varphi_0}\delta^i_j = T^i_{\ j} = \left(\frac{1}{2}\dot{\varphi}_0^{\ 2} - V(\varphi_0)\right)\delta^i_j. \tag{2.21}$$

A homogeneous scalar field works as a relativistic perfect fluid [5]. But the main feature that we are interested in is the fact that the potential has opposite signs in the RHSs of Eq. (2.21) and Eq. (2.20). So if

$$V(\varphi_0) > \dot{\varphi}_0^{\ 2}, \tag{2.22}$$

the condition in Eq. (2.7) is satisfied and inflation starts.

One might question how likely is that a generic scalar field respect the last condition. If its potential has a plateau big enough, Eq. (2.22) is actually an attractive solution. In fact if the field is on the plateau it means that the scalar energy density due to the potential is approximately constant as the Universe expands. On the other hand using 2.6 on the scalar field kinetic energy alone, i.e. by neglecting the potential in Eq. (2.21) and Eq. (2.20), we could see that the kinetic term is washed away really fast as the Universe expand [5]. The same thing applies to the densities of other matter and gauge fields. So if we require that the potential in flat enough, the expansion guarantees that eventually the inflaton can reach the condition

$$V(\varphi_0) \gg \frac{1}{2}\dot{\varphi}_0^{\ 2}. \tag{2.23}$$

This is called slow roll condition. In this case we obtain $\rho_{\varphi_0} \approx V(\varphi_0)$ and $p_{\varphi_0} \approx -V(\varphi_0)$, i.e. a de Sitter inflation.

During slow roll, we can plug the expressions of the scalar field energy density (Eq. (2.20)) in the first Friedmann equation (2.4)

$$H^2 \approx \frac{8\pi G}{3}V(\varphi_0). \tag{2.24}$$

Again during slow roll, in the Klein-Gordon equation (2.19) the friction term suppresses $\ddot{\varphi}_0$

$$\ddot{\varphi}_0 \ll 3H\dot{\varphi}_0, \tag{2.25}$$

$$3H\dot{\varphi}_0 \approx -V'(\varphi_0). \tag{2.26}$$

To characterize the slow roll conditions Eq. (2.23) and (2.25), one can introduce the so called slow-roll parameters

$$\epsilon \equiv \frac{1}{16\pi G}\left(\frac{V'}{V}\right)^2 \approx \frac{\dot{H}}{H^2}, \tag{2.27}$$

$$\eta \equiv \frac{1}{8\pi G}\left(\frac{V''}{V}\right) = \frac{1}{3}\frac{V''}{H^2}, \tag{2.28}$$

which give information on the shape of the inflaton potential and are useful to study the inflaton dynamics. Equations 2.23 and 2.25 are equivalent to require $\epsilon, |\eta| \ll 1$.

Now we investigate the quantum fluctuations of the inflaton field. As we will see those fluctuations are important because they can explain the presence and the properties of the primordial density fluctuations. We can see them as the seeds of cosmic structure growth.

We can use Eq. (2.17) in the Klein-Gordon equation, and Taylor-expand the inflaton potential

$$\ddot{\varphi}_0 + \ddot{\delta\varphi} + 3H\dot{\varphi}_0 + 3H\dot{\delta\varphi} - \frac{\nabla^2\delta\varphi}{a^2} = -V'(\varphi_0) - V''(\varphi_0)\delta\varphi + \dots. \tag{2.29}$$

Using the Klein-Gordon for the background we get the equation of motion for the fluctuations at first order

$$\ddot{\delta\varphi} + 3H\dot{\delta\varphi} - \frac{\nabla^2\delta\varphi}{a^2} = -V''(\varphi_0)\delta\varphi. \tag{2.30}$$

We can solve it using a fixed time 3D Fourier transform in a flat space.

$$\delta\varphi(\mathbf{x}, t) = \int \frac{d^3k}{(2\pi)^3} \delta\varphi_{\mathbf{k}}(t) e^{i\mathbf{x}\cdot\mathbf{k}}. \tag{2.31}$$

The different modes decouple and the equation becomes

$$\ddot{\delta\varphi}_{\mathbf{k}} + 3H\dot{\delta\varphi}_{\mathbf{k}} + \frac{k^2\delta\varphi}{a^2}\delta\varphi_{\mathbf{k}} = 0, \tag{2.32}$$

where we also used the slow roll condition $V'' \ll H^2$ to suppress the RHS.

Now that we have written in Fourier space the equation of motion we want to solve, we can apply second quantization. It is convenient to use the conformal time defined by

$$d\tau \equiv \frac{dt}{a(t)}, \tag{2.33}$$

and in the following we will mark derivative with respect to the conformal time with a prime '. We also renormalise the fluctuation field as

$$\widehat{\delta\varphi} = a\delta\varphi. \tag{2.34}$$

Then

$$\widehat{\delta\varphi}(\mathbf{x}, \tau) = \int \frac{d^3k}{(2\pi)^3}\left[u_{\mathbf{k}}(\tau)a_{\mathbf{k}}e^{i\mathbf{x}\cdot\mathbf{k}} + u_{\mathbf{k}}^*(\tau)a_{\mathbf{k}}^\dagger e^{-i\mathbf{x}\cdot\mathbf{k}}\right], \tag{2.35}$$

with the commutation relations

$$[a_{\mathbf{k}}, a_{\mathbf{k}'}] = 0, \qquad \left[a_{\mathbf{k}}, a_{\mathbf{k}'}^{\dagger}\right] = \hbar \, \delta^{(3)}(\mathbf{k} - \mathbf{k}'), \tag{2.36}$$

and the normalization condition

$$u_{\mathbf{k}}^* u_{\mathbf{k}}' - u_{\mathbf{k}}(u_{\mathbf{k}}^*)' = -i. \tag{2.37}$$

We use the Bunch-Davies vacuum choice, i.e. the quantum fluctuations must reduce to quantum field theory in flat space-time on very small physical scales

$$u_{\mathbf{k}}(\tau) \xrightarrow[k \gg aH]{} \frac{e^{i\tau k}}{\sqrt{2\omega_k}}. \tag{2.38}$$

From Eq. (2.32) we get

$$u_{\mathbf{k}}''(\tau) + \left(k^2 - \frac{a''}{a} + V''a^2\right) u_{\mathbf{k}}(\tau) = 0. \tag{2.39}$$

Using the two slow roll parameters defined in Eq. (2.27) and (2.28) we can rewrite this last equation in the form of a Bessel equation. In fact we can write two expressions

$$\frac{a''}{a} = \frac{2}{\eta}(1 + \frac{3}{2}\epsilon + O(\epsilon^2, \eta^2)), \tag{2.40}$$

$$V''a^2 = 3a^2 H^2 \eta \tag{2.41}$$

that plugged into Eq. (2.39) give

$$u_{\mathbf{k}}''(\tau) + \left(k^2 - \frac{\nu^2 - 1/4}{\tau^2}\right) u_{\mathbf{k}}(\tau) = 0, \tag{2.42}$$

with

$$\nu = \frac{3}{2} + \epsilon - \eta. \tag{2.43}$$

This is the expression of the Bessel equation up to first order in ϵ and η, as it requires ν to be a constant and it could be shown that $\dot{\epsilon}/(H\epsilon) = O(\epsilon^2)$ [5].

When talking about the evolution of the classical background field we said that we could safely use the background FRW metric. At first order in the slow-roll parameters it is not true any more as the perturbations of the metric lead to first order corrections. Taking them into account as in [5] we would end up with a different dependence on the slow-roll parameters

$$\nu = \frac{3}{2} + 3\epsilon - \eta. \tag{2.44}$$

However the solution of the Bessel equation is known to be

$$u_{\mathbf{k}}(\tau) = \sqrt{\tau} \left[c_1(k) \, H_\nu^{(1)}(-k\tau) + c_2(k) \, H_\nu^{(2)}(-k\tau)\right], \tag{2.45}$$

where $H_\nu^{(1,2)}$ are the Henkel functions of the first and second kind. Their asymptotic expansions are

$$H_\nu^{(1)}(X \gg 1) \approx \left(H_\nu^{(2)}\right)^* (X \gg 1) \approx \sqrt{\frac{2}{\pi X}} \exp\left[i\left(X - \frac{\nu\pi}{2} - \frac{\pi}{4}\right)\right]. \qquad (2.46)$$

Notice that in the limit $k\tau \gg 1$ we are considering small scales, so by comparing with the Bunch-Davies Eq. (2.38) we obtain

$$u_{\mathbf{k}}(\tau) = \frac{\pi}{2}e^{i\left(\frac{\nu\pi}{2} - \frac{\pi}{4}\right)}\sqrt{-\tau}H_\nu^{(1)}(-k\tau). \qquad (2.47)$$

On small scales quantum fluctuations of the inflaton are approximated by the usual flat space-time quantum field theory. Now we describe the dynamics on bigger scales.

When we firstly introduced inflation we said it is a phase of accelerated expansion of the Universe, $\ddot{a} > 0$. The acceleration implies a decrement of the comoving Hubble horizon $(aH)^{-1}$, which is the scale beyond which causal processes cannot operate. During inflation the expansion stretches the wavelength of quantum fluctuations whilst the Hubble radius shrink, so eventually fluctuations could cross the horizon. The amplitude of the fluctuations on super-horizon scales then remains almost unchanged for a very long time, as we will further discuss, whereas their wavelengths still grow exponentially. A given scale that exited the Hubble horizon during inflation could eventually re-enter after the end of the inflation, when horizon start to expand (see figure 2.1).

To study large scales we can take the Henkel function expansion in the small argument limit

$$H_\nu^{(1)}(X \ll 1) \approx \sqrt{\frac{2}{\pi}}e^{\frac{-i\pi}{2}}2^{\nu - \frac{3}{2}}\frac{\Gamma(\nu)}{\Gamma(3/2)}X^{-\nu}, \qquad (2.48)$$

and rescaling to the $\delta\varphi_{\mathbf{k}}$ field, we obtain

$$|\delta\varphi_{\mathbf{k}}| = 2^{\nu - \frac{3}{2}}\frac{\Gamma(\nu)}{\Gamma(3/2)}\frac{H}{\sqrt{2k^3}}\left(\frac{k}{aH}\right)^{\frac{3}{2} - \nu}. \qquad (2.49)$$

Non zero slow-roll parameters, i.e. a non completely flat inflaton potential, make fluctuations scale dependent.

To study fluctuations it is useful to introduce the power spectrum $P(k)$. For a generic field $\delta(\mathbf{x}, t)$ this is defined as

$$\langle\delta_{\mathbf{k}}(t)\delta_{\mathbf{k}'}(t)\rangle \equiv (2\pi)^3 P(k,t)\delta^{(3)}(\mathbf{k} - \mathbf{k}'). \qquad (2.50)$$

Related to it we can define a dimensionless power spectrum

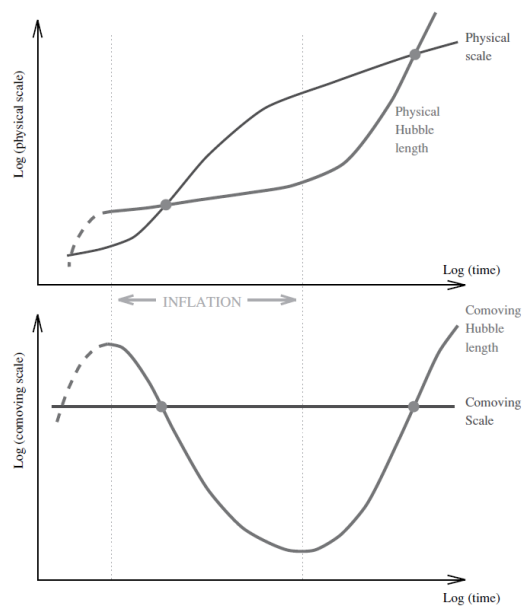$$\mathcal{P}(k) \equiv \frac{1}{2\pi^2}k^3 P(k). \qquad (2.51)$$

Figure 2.1: Two views of the size of a comoving region within the observable Universe, relative to the Hubble length (horizon scale). The comoving Hubble horizon is decreasing during inflation and increases afterwards. The upper panel shows the physical size of the region, the lower panel its comoving size. The vertical axis covers many powers of 10 in scale. The region starts well inside the horizon, then crosses outside some time before the end of inflation, re-entering long after inflation is over. Figure from [4]

Finally we define the (scalar) spectral index

$$n - 1 \equiv \frac{d \ln \mathcal{P}(k)}{d \ln k}.$$

(2.52)

We can easily evaluate the power spectrum for the inflaton field fluctuations at lowest order in slow-roll parameters. By definition

$$\langle \delta\varphi_{\mathbf{k}}(t)\delta\varphi_{\mathbf{k}'}(t)\rangle \equiv (2\pi)^3 P_{\delta\varphi}(k)\delta^{(3)}(\mathbf{k} - \mathbf{k}').$$

(2.53)

By explicit calculation

$$\langle \delta\varphi_{\mathbf{k}}(t)\delta\varphi_{\mathbf{k}'}(t)\rangle \propto |\delta\varphi_{\mathbf{k}}|^2 \delta^{(3)}(\mathbf{k} - \mathbf{k}')$$

(2.54)

so

$$P_{\delta\varphi}(k) = |\delta\varphi_{\mathbf{k}}|^2$$

(2.55)

and, by Eq. (2.49) we obtain

$$\mathcal{P}_{\delta\varphi} = \left(\frac{H}{2\pi}\right)^2 \left(\frac{k}{aH}\right)^{3-2\nu}.$$

(2.56)

By now everything is pretty much clear. What we miss is a link between quantum perturbations that have occurred during inflation and primordial density perturbations that were the seeds of all the cosmic structure we see today.

The easiest way to approach the problem is to introduce the curvature perturbation on uniform density hypersurfaces (see [6] or the more recent [7])

$$\zeta \equiv -\psi - \frac{H\delta\rho}{\dot{\rho}}$$

(2.57)

where ψ is the scalar perturbation of the diagonal spatial component of the metric. In this discussion we choose the uniform curvature gauge, in which $\psi = 0$. ζ is a gauge invariant quantity [7], and has the fundamental property of being constant on super horizon scales in the case of interest [5].

So for each k, we can evaluate the quantum density fluctuation at the horizon crossing, i.e. $k \approx aH$. From that we can calculate ζ, and since the latter is constant super horizon we know its amplitude even when the chosen k re-enters the horizon during radiation or matter domination. In this way we can easily compute the energy density perturbation after inflation at a given scale. Using Eq. (2.6) and (2.26) in Eq. (2.57) we get

$$\zeta = -\frac{H\delta\varphi}{\dot{\varphi}}.$$

(2.58)

To fix ideas we can consider a mode that re-enters the horizon during radiation domination. Then

$$\zeta = \frac{\delta\rho_{\mathrm{rad}}}{4\rho_{\mathrm{rad}}}.$$

(2.59)

The two last equations can be equated if evaluated upon exiting and re-entering the horizon, say at times $t(k)_{\text{ex}}$ and $t(k)_{\text{en}}$ respectively.

Now we can finally define the primordial power spectrum (PPS) as the power spectrum of the density perturbations

$$\mathcal{P}_\zeta = \left(\frac{H^2}{2\pi\dot\varphi} \right)^2 \Bigg|_{t(k)_{\text{ex}}} . \tag{2.60}$$

To know its dependence on the inflaton potential shape, we can check its spectral index. Using the relation $d\ln k \approx H\,dt$ it results that

$$n_s - 1 = \frac{d\ln\mathcal{P}_\zeta}{d\ln k} = -2\frac{\ddot\varphi}{H\dot\varphi} + 4\frac{\dot H}{H^2} = 2\eta - 6\epsilon. \tag{2.61}$$

Usually the PPS is shown writing explicitly its dependence on k. Since at first order the slow roll parameters are constant the PPS is a power law

$$\mathcal{P}(k) = A_s \left(\frac{k}{k_0} \right)^{n_s - 1} \tag{2.62}$$

where A_s and n_s are two constants and k_0 is a pivot scale, usually set at $k_0 = 0.02h/\text{Mpc}$. This simple model fits data to a very high accuracy [1]. For the best fit value of the parameters we refer to table 1.1. As experimental evidence support $n_s = 0.9645 \pm 0.00490$, the PPS is said to have a red tilt, as it cuts power at higher momenta.

We got our prediction on the power law shape of the PPS from the assumption that the slow roll parameters were little and for this reason almost constant. Experiments like WMAP and *Planck* checked for the presence of deviations. The first considered is a running of n_s, $d\ln n_s/d\ln k$. Other relevant deviations could be features, more or less localized around some peculiar k, in the PPS. For example they could be oscillations or bumps superimposed to the known power law. *Planck* had not found evidence of the running or of any feature [8]. With our work we hope to give a second point of view on this topic, adding to the analysis LSS surveys data.

Chapter 3

Theoretical Models

In the previous section we described how a smooth inflaton potential, for which the slow roll parameters are almost constant, generates a power law power spectrum. That picture is strongly supported by the results of the *Planck* satellite observations [8]. However a lot of other inflationary models fit the same set of data, usually at the price of introducing more free parameters. Although those models are generally disfavoured by Bayesian evidence [8], it is still important to explore all the possible signatures of inflation. Moreover a joint analysis of *Planck* and LSS surveys has never been used to reconstruct the PPS and this is the main goal of this thesis. If in *Planck* data there is no strong hint of the presence of features, adding other datasets could turn the tables, as more sophisticated models could improve the fit results. Most theoretical inflationary models albeit based on very different underlying physics, generate features that could be grouped in 3 main classes [8]. In the subsequent sections we briefly review how different shapes of the inflaton potential reflects on different modulation of the PPS. Should our reconstruction show a deviation from the power law in 2.62, knowing the zoology of inflationary models will be useful to eventually find a primordial origin of the deviation. The typical shape of the PPS generated by each class of model is presented in figure 3.1.

3.1 Step features

If the inflaton potential is not completely smooth, but instead has a localized step-like feature, when the inflaton crosses it the slow roll parameters suddenly increase. If the step is not to big or sharp inflation do not end – i.e. if the condition Eq. (2.7) is still satisfied – but the power spectrum is affected indeed. In Ref. [9] it is given a description of both a step in the sound speed and in the potential of the inflaton field is given.

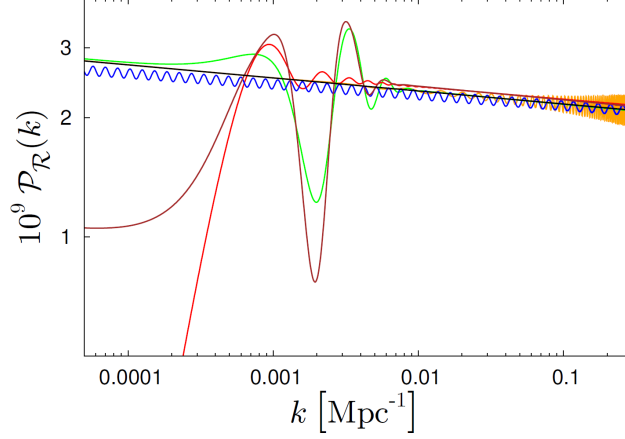This analysis covers models based on a Dirac-Born-Infeld Lagrangian of the

Figure 3.1: Best fit power spectra for the power-law (black curve), step (green), loga-rithmic oscillation (blue), linear oscillation (orange), cut-off (red) and a step in both the warp and the potential (brown). The last two models are not reviewed here. The figure is taken from ref. [8].

type

$$\mathcal{L} = \left(1 - \sqrt{1 + (\partial^\mu \phi \partial_\mu \phi)/T(\phi)}\right) T(\phi) - V(\phi), \tag{3.1}$$

where

$$T(\phi) = \frac{\phi^4}{\lambda_B}(1 + b_T F(\phi)), \tag{3.2}$$

and

$$V(\phi) = V_0(1 - \frac{1}{6}\beta\phi^2)(1 + b_V F(\phi)). \tag{3.3}$$

Here λ_B, V_0, and β are free parameters describing the background evolution, while b_T and b_V parametrize the step depth. $F(\phi)$ is a step function, hereafter we will consider the case of an hyperbolic tangent.

The contribution of the step feature to the Bessel equation 2.42 can be con-sidered as an external source. It can be solved iteratively improving the solution for the presence of the deviations introduced by the step. The power spectrum is

$$\mathcal{P}(k) = A_s \left(\frac{k}{k_0}\right)^{n_s - 1} \exp\left[I_0(k) + \ln\left(1 + (I_1(k))^2\right)\right], \tag{3.4}$$

where the leading contribution from the step is

$$I_0(k) = \left[C_1 W(ks_{\text{st}}) + C_2 W'(ks_{\text{st}}) + C_3 Y(ks_{\text{st}})\right] \mathcal{D}\left(\frac{ks_{\text{st}}}{x_{\text{st}}}\right), \tag{3.5}$$

and on the second iteration the correction is

$$\sqrt{2} I_1(k) = \frac{\pi}{2}(n_s - 1)\left[C_1 X(ks_{\text{st}}) + C_2 X'(ks_{\text{st}}) + C_3 Z(ks_{\text{st}})\right] \mathcal{D}\left(\frac{ks_{\text{st}}}{x_{\text{st}}}\right). \tag{3.6}$$

Here s_{st} is the sound horizon when the inflaton crosses the step, and x_{st} is related to the width of the step. However we can simply think of them as two free parameters. The window functions are defined as

$$
\begin{aligned}
W(x) &= \frac{3\sin(2x)}{2x^3} - \frac{3\cos(2x)}{x^2} - \frac{3\sin(2x)}{2x} \\
X(x) &= \frac{3}{x^3}(\sin x - x\cos x)^2 \\
Y(x) &= \frac{6x\cos(2x) + (4x^2 - 3)\sin(2x)}{x^3} \\
Z(x) &= -\frac{3 + 2x^2 - (3 - 4x^2)\cos(2x) - 6x\sin(2x)}{x^3}.
\end{aligned}
\tag{3.7}
$$

The explicit expression of W' is

$$
W' = \frac{1}{2x^4}[\cos(2x)(18x - 6x^3) + \sin(2x)(15x^2 - 9)]
$$

and the damping factor is

$$
\mathcal{D}(y) = \frac{y}{\sinh(y)}.
\tag{3.8}
$$

For a simpler scenario with a potential-only step and canonical sound speed $c_s = 1$, we have $C_1 = 0 = C_3$.

The best fit for *Planck* is shown in figure 3.1.

3.2 Oscillating features

Linear oscillations typically occurs in boundary effective field theory models [8, 10]. Usually the oscillation itself has some sort of power law damping. It can be parametrized as

$$
\mathcal{P}(k) = A_s \left(\frac{k}{k_0}\right)^{n_s - 1} \left[1 + \frac{C_{\text{lin}}}{\Lambda}\left(\frac{k}{k_0}\right)^{n_{\text{lin}}}\cos\left(\omega_{\text{lin}}\frac{k}{k_0} + \phi_{\text{lin}}\right)\right],
\tag{3.9}
$$

the symbols with the "lin" subscript are the free parameters. The best fit for *Planck* is shown in figure 3.1.

3.3 Logarithmically oscillating features

Due to the (almost) exponential growth of the scale factor during inflation, every source of perturbation which is periodic would produce logarithmically oscillating features in the PPS. Some examples could be an inflaton potential with a sinusoid superimposed to the flat potential that drives inflation, or oscillating heavy scalar field that coexisted with the inflation driving field [11]. Another example to

which we will stick to fix ideas comes from models that propose vacuum choices different from the Bunch Davies in Eq. (2.38). Those theories question the fact that the quantum fluctuations are supposed to originate in the infinite past with an infinitely short wave length (Ref. [12]). Setting the initial condition on arbitrarily small scales contrasts with the fact that quantum mechanics could not work well on scales that are smaller than the Planck length. In fact we can call Λ the energy scale of new physics, and ask for a vacuum choice that is well defined on $k \approx \Lambda$ instead that for $k \longrightarrow \infty$ as implicitly required in Eq. (2.38).

Considering the scale Λ at which current physics understanding fails in the choice of the vacuum, we could modify calculations in chapter 2 as in [12], to end up with the inflaton power spectrum

$$P_\phi(k) = \left(\frac{H}{2\pi}\right)^2 \left[1 - \frac{H}{\Lambda} \sin\left(\frac{2\Lambda}{H}\right)\right]. \tag{3.10}$$

Then for the very same calculation already performed we would obtain [10]

$$\mathcal{P}(k) = A_s \left(\frac{k}{k_0}\right)^{n_s - 1} \left[1 + \frac{C_{\log}}{\Lambda} \cos\left(\omega_{\log} \ln\left(\frac{k}{k_0}\right) + \phi_{\log}\right)\right], \tag{3.11}$$

where again the symbols with the "log" subscript are the free parameters. The best fit for *Planck* is shown in figure 3.1.

Chapter 4

Primordial Power Spectrum Reconstruction

We perform a minimally-parametric reconstruction of the primordial power spectrum based on the method of ref. [13]. Since the ΛCDM concordance model makes use of a power-law PPS, we focus our search on small and smooth deviation from a power-law. We use a cubic smoothing spline technique to parametrize the power spectrum (section 4.1). Cubic spline allows to create various shapes with a finite set of parameters. To find out which are the right values to assign to those parameters we use a Monte Carlo Markov Chain (section 4.2). This is done with the codes CLASS and Monte Python (section 4.4).

4.1 Smoothing Splines

The goal we defined is to recover a smooth function $P(k)$ given its value at specified points. Let's say we have n different points. We know that we can always define a polynomial of degree $n-1$ which pass for each point. This kind of approach is not quite satisfactory if we are trying to recover a smooth signal. In fact for big n it gives rise to an unnecessarily wiggly curve. There is a way to find the "most straight" function with a given order of continuous derivatives. It is to use splines. We can define a spline of degree k $S(x)$ as a function such that

1. $S(x)$ is well defined on $x \in [a, b]$

2. $S(x)$ and its derivatives $S'(x), S''(x), \ldots, S^{(k-1)}(x)$ are continuous for $x \in [a, b]$

3. $\exists\, x_0, \ldots, x_n$ such that $a = x_0 < x_1 < \cdots < x_n = b$ and $S(x)$ is a polynomial of degree at most k on $[x_{i-1}, x_i]$ $i = 1, \ldots, n$

It could be shown that a cubic spline is the "best" interpolating curve one can find among all the functions $f \in \mathcal{C}^2$ interpolating all the points, in the sense it is

the one that minimizes $\int (f''(x))^2 dx$ in the domain [14]. Since this integral can intuitively be associated to the notion of straightness, we can say a cubspl is the straightest interpolating curve.

The points $(k, P(k))$ that we wish to interpolate are called knots. Given $n+1$ knots n intervals are defined so we will need $4n$ parameters to define a cubic in each interval. We can impose $2n$ conditions asking that each cubic pass for the knots at the beginning and the end of the interval in which it is defined. Other $2(n-1)$ conditions come from the request of continuity of first and second derivative. Then we are left with 2 degrees of freedom we have to deal with. Depending on the problem we want to solve there are different possible choices. In the present work we will use spline to reconstruct the PPS. The parameters that completely define it, and which we will need to determine are the PPS value on knots. As we will explain more in detail in chapter 5, for our numerical analysis we will use five parameters. To avoid computational inefficiencies we will use splines with two extra knots at each of the spline ends. Since those two extra knots are not directly involved in our simulation, and are indeed function of the other knots, we will address to them as *false* knots in the following. Then the natural choice to deal with the last two degrees of freedom a spline has is the *not-a-knot* condition. The jump in the third derivative across the first and last *real* knots is forced to zero. This way the cubic polynomial pieces at the left and right of said knots are made to coincide. The spline is constructed using C. de Boor's algorithm, and his own code [14].

4.1.1 Working in logarithmic space

As we already discussed, the signal we try to recover is expected to be a small deviation form a power law. A power law as in Eq. (2.62) can be linearised by taking the logarithm of both sides

$$\log \mathcal{P}(k) = \log A_s + (n_s - 1)[\log(k) - \log(k_0)]. \tag{4.1}$$

Small deviations on the power law translate into small deviation on this linearised expression.

The advantage is that splines approximate the linear expression way better than the original one. It is really evident checking both figure 4.1 where a spline is used to approximate a power law and figure 4.2 where a little bump is added to a power law.

Furthermore the same procedure has already been applied in literature, e.g. [13].

4.2 Inference and Monte Carlo Markov Chains

Let's assume there is a theory defined by a set of parameters $\boldsymbol{\alpha}_{true}$. They are statistically realized in our observable Universe, i.e. they can be obtained by
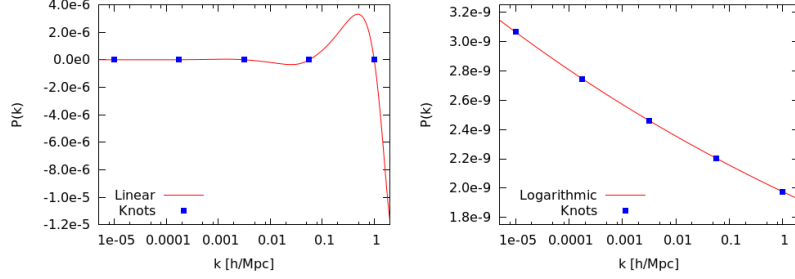
Figure 4.1: Splines interpolating mock knots placed alongside a power law signal. On the left the spline is a function of k taken in linear space, on the right in logarithmic space. Notice the difference in the scale.
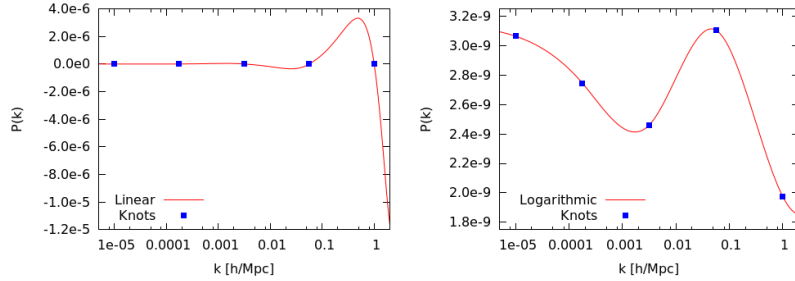

Figure 4.2: Splines interpolating mock knots placed alongside a power law signal with a bump in it. On the left the spline is working in linear space, on the right in Logarithm space. Notice the difference in the scale.

averaging over the ensemble of possible universes from the underlying theory. As we can observe only our Universe, we got access to a single set of measured data $\mathcal{D}_0$, which is of course affected by errors, and depends on our Universe realization of the true parameters, rather than on the true parameters themselves. From this set of data we can infer which is the best estimate $\boldsymbol{\alpha}_0$ of the parameters in our specific Universe. We can imagine that living in another hypothetical universe we would have measured different data $\mathcal{D}_i$ $i = 1, 2, \ldots$ which would have led to different $\boldsymbol{\alpha}_i$ $i = 1, 2, \ldots$. If it was possible to measure all the $\boldsymbol{\alpha}_i$ we could take their mean to find $\boldsymbol{\alpha}_{true}$ from the definition of ensemble. Moreover we would know the distribution of $\boldsymbol{\alpha}_i - \boldsymbol{\alpha}_{true}$. That is the only thing we need if we want to know everything about the uncertainties of our estimate $\boldsymbol{\alpha}_0$. However we do not have access to the ensemble of all possible universes. We thus need a way to discover the distribution $\boldsymbol{\alpha}_i - \boldsymbol{\alpha}_{true}$ without knowing $\boldsymbol{\alpha}_{true}$.

The probability of an hypothesis, i.e. our set of parameters $\boldsymbol{\alpha}$, given the data we have collected $\mathcal{D}$ is given by the Bayes' theorem

$$\mathcal{P}(\boldsymbol{\alpha}, \mathcal{D}) = \frac{\mathcal{P}(\mathcal{D}, \boldsymbol{\alpha})\mathcal{P}(\boldsymbol{\alpha})}{\mathcal{P}(\mathcal{D})}. \tag{4.2}$$

In Bayesian probability the quantity on the LHS is called posterior. The likelihood $\mathcal{P}(\mathcal{D}, \boldsymbol{\alpha})$ is the probability of obtaining the measures $\mathcal{D}$ in an universe where the true parameters are known to be $\boldsymbol{\alpha}$. The quantity $\mathcal{P}(\mathcal{D})$ at the denominator is the probability of getting the considered data. Since in our case some experiments already took the measures we are talking about, we can consider this quantity as just a normalization. Finally $\mathcal{P}(\boldsymbol{\alpha})$ is the prior. It represent the state of knowledge we had before seeing the data; for example it could contain information from previous experiments or theoretically supported constraints.

Bayesian inference on the parameter $\boldsymbol{\alpha}$ is performed studying the posterior. Once the posterior distribution is known one can choose a statistic (the mean, the median, ...) to determine an estimator $\hat{\boldsymbol{\alpha}}$ that is the final guess for the true parameter $\boldsymbol{\alpha}_{\text{true}}$. We will work with a maximum likelihood inference: our estimator will be the choice of parameters that maximise the likelihood.

There are two difficulties in Bayesian inference. The first one lies in the arbitrariness of the choice of the prior, but we will not address to the problem here (see [15] for a discussion on the topic). The second is that an expression for the likelihood in generally unknown. The solution is to use numerical methods to evaluate the likelihood and draw a sample from the posterior. An appropriate technique to use is called Markov Chain Monte Carlo [16].

MCMC [17] are useful because they can map high dimensional likelihood space in an efficient and accurate way. By comparison, the evaluation time for a grid of fixed spacing scales exponentially with the number of dimension and the grid doesn't adjust to get more precision where is needed. On the other hand MCMC scales approximately linearly with the number of parameters and has a larger point density in places where the likelihood is bigger, thus giving more accuracy around the maxima, which eventually are what we are interested in. The idea is by no means different to a hit or miss Monte Carlo integration: in this kind of process the integral is proportional to the ratio of accepted points over the total number of tries.

The MCMC evaluate the posterior of points in the parameter space to draw a random walk in which the probability of being in a point is proportional to the posterior.

In order to achieve this result one has to face two problems. The first is tied with the arbitrariness of the starting point. Every chain starts going through a burn-in period during which its motion is highly chaotic and highly dependent on the starting point. After this period it becomes approximately stationary and loses its dependence from the start. We can say it has converged. We will need a method to select the burn-in and remove it from the data we are interested in. The second problem is that a finite-size chain cannot explore all the areas of the parameter space. Given enough time ergodicity guarantees that the chain will cover all the target distribution, but it is important to set the length of the steps in such a way that it doesn't take too much time for the chain to cover the whole

parameter space. A chain which does this well is said to have a good mixing.

The Metropolis Hastings algorithm is a simple implementation of MCMC. It's composed of the following steps.

1. It starts with a set of parameters $\boldsymbol{\alpha}_1^S$ and it computes the associated likelihood $\mathcal{L}_1 = \mathcal{L}(\mathcal{D}, \boldsymbol{\alpha}_1^S)$.

2. It takes a random step in parameter space following in every direction a Gaussian distribution. Its σ is called step size, and is correlated to the goodness of the mixing as we anticipated. Let $\boldsymbol{\alpha}_2^S$ be the arrival point.

3. compute the likelihood $\mathcal{L}_2 = \mathcal{L}(\mathcal{D}, \boldsymbol{\alpha}_2^S)$.

4.a. If $\mathcal{L}_2/\mathcal{L}_1 \geq 1$ the point is accepted because it improves the likelihood and saved in the chain. Then it goes back to step 2 using the new point.

4.b. If $\mathcal{L}_2/\mathcal{L}_1 < 1$ a random number x is drawn from a uniform distribution in $[0, 1]$. If $\mathcal{L}_2/\mathcal{L}_1 \geq x$ the point is accepted despite it decreases the likelihood and saved in the chain. If $\mathcal{L}_2/\mathcal{L}_1 < x$ the new point is discarded and $\boldsymbol{\alpha}_1^S$) is saved a second time. Then it goes back to step 2 using the new point.

4. Four or more chains are started in different well spaced points. When the convergence criterion we will discuss in a moment is satisfied and the chains have enough points to provide a good sample of the posterior, the chains are stopped.

When running a chain we need to know when it has converged and if it has explored the whole parameter space. Gelman & Rubin proposed the following method to do this [18]. M chains are started in different points in parameter space, and every of them collects 2N steps. The first N are discarded as burn in. Now we can refer to the i-th element of the j-th chain as y_i^j with $i = 1, \ldots, N$ and $j = 1, \ldots, M$. Notice that y_i^j, being a point a parameter space is indeed a vector and the following holds for each of its components, i.e. for each cosmological parameter we are testing.

The mean of the j-th chain is

$$\bar{y}^j = \frac{1}{N} \sum_{i=1}^{N} y_i^j \tag{4.3}$$

and the mean of the sample is

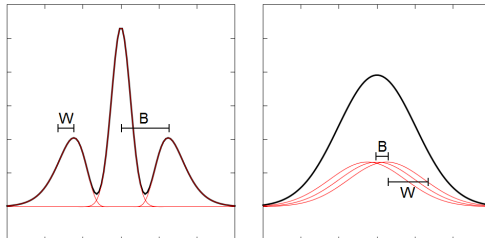$$\bar{y} = \frac{1}{N\,M} \sum_{i,j=1}^{N,M} y_i^j. \tag{4.4}$$

Figure 4.3: Pictorial representation of the idea underlying the Gelman-Rubin criteria. On the left side 3 chains that haven't explored the parameter space properly. On the right side the same chains when they begin to converge

Then the variance between the chains is

$$B = \frac{1}{M-1} \sum_{j=1}^{M} (\bar{y}^j - \bar{y})^2 \tag{4.5}$$

and the mean of the variances within single chains

$$W = \frac{1}{M(N-1)} \sum_{i,j=1}^{M,N} ((y_i^j - \bar{y}^j)^2. \tag{4.6}$$

Then we can define the ratio between two estimates of the variance of the distribution

$$R = \frac{\frac{N-1}{N}W + (1 + \frac{1}{M})B}{W}. \tag{4.7}$$

The numerator is an unbiased estimator of the variance if the distribution is stationary, but is otherwise an overestimation. On the other hand the denominator underestimates the variance if the individual sequences haven't converged yet. In figure 4.3 we give a qualitative representation of the quantities used to compute R.

During the run of the chain R is computed and recorded. We can be quite sure that the chain converged when the value of R starts to be always < 1.03.

Once we are sure the chain converged the burn-in are discarded and what is left is merged together. By construction the "punctual" density of the chains point in parameter space is proportional to the posterior probability of said point. Once we have the posterior we can easily deduce best fit parameters and confidence levels.

In practice we apply Bayesian inference to the four cosmological parameters ω_b, ω_{cdm}, h, and τ_{reio}, and to the values of the five knots amplitude. With the results of the MCMC we obtain the best fit of the cosmological parameters, and jointly the shape of the spline that parametrize the PPS.

4.3 Cross-Validation

Up to now we introduced a way to reconstruct the primordial power spectrum given a class of experimental data. But how can we be sure that our reconstruction is the correct one? For sure trying to maximise the likelihood would be a good start. If experimental data were noiseless we would have finished indeed, but this is not the case. There is a very high chance that we are, at least in part, fitting the noise. To be precise, if only one dataset is given, we can be sure that the best fit would be the one that fits signal and noise both, and not the one that only fit the signal and not the noise. This is so because with only one dataset there is no way to tell the signal and the noise apart. To prevent this behaviour we add a roughness penalty to the logarithm of the likelihood. It is a function that increases its value as much as the spline gets more and more wiggly. Our choice is the integral of the second derivative squared of the spline that has to be added to the logarithm of the likelihood. As we are working in logarithmic scale, the integral is taken in respect to $\ln k$ as well

$$\log(\mathcal{L}) = \log(\mathcal{L}_{exp}) + \alpha_p \int_{\ln k_i}^{\ln k_f} (S(\ln k))^2 \, d\ln k \qquad (4.8)$$

where k_i and k_f are respectively the position of the first and of the last knots, and α_p is a weight that controls the penalty on the roughness. The choice of α_p value affects the straightness of the spline. For $\alpha_p = 0$ we go back to finding the best fit for the data without caring about signal and noise distinction. For $\alpha_p \to \infty$ a straight line will be favoured, and the fit will become a linear regression. This is where cross-validation comes into play [19]. The idea is to divide available data in two groups, fit the first group with a chosen value for α_p and try to see how well the fit results approximates the other data group. If the fit is correct it will predict in an accurate way the second group. Ideally the most rigorous way to use cross-validation would be to remove one point at a time and evaluate the discrepancy between the point and its prediction. Each of those errors are summed in a value called cross-validation score. The correct α_p is chosen as the one that minimizes the CV score.

In practice removing one point at a time implies repeating the analysis as many times as the number of points, so it is too computationally expensive. As done in [13], we will split data in only two sets, lets say CV_A and CV_B, in such a way that all data from each evaluated experiment goes into one set. The cross-validation score is computed by evaluating both the minus log likelihood of CV_B given the best fit of CV_A, let's call it CV_{AB}, and the reverse CV_{BA}, and adding them. As said before, the correct value for α_p will be the one that minimizes $CV_{AB}+CV_{BA}$.

In this way, using different combinations of experiments in CV_A and CV_B, we can not only check if our reconstruction is right, but also if some experiments lead to a PPS which is inconsistent with the others. Let's say we got two compatible

experiments 1, 2 and a third experiment 3 affected by some previously unknown systematics or physical effects. We could arrange the experiments in the two cross-validation sets in various configurations. What we would see is that every set of parameter fitted on 3 would fail in predict the data in 1 and 2. Cross-validation score would be much bigger, giving a warning that there is some newly introduced tension between the data. From there we can draw our conclusion on the fact that the experiment 3 analysis is missing something. Of course, simplistic examples aside, it won't be possible to spot the "right" and the "wrong" data, as it is entirely possible that 1 and 2 are biased instead.

4.4   CLASS and Monte Python

4.4.1   CLASS and code development

Up to now we explained how we can reproduce a whole primordial power spectrum in a minimally parametric way, writing it as a function of few parameters. Then we discussed how to find the best value for said parameters studying the posterior. What's left is to describe how to actually calculate the likelihood given a set of parameters. It is indeed a non trivial problem at all. To measure is always a delicate problem, even if it is made directly. Moreover in cosmology we are not so lucky. We have to do indirect measurements of the parameters of interest. What we can see is not the primordial power spectrum at all. If it was it wouldn't be called primordial indeed. What it was in the beginning has been stretched and enlarged and damped non homogeneously by billions years of ageing. During all this time the original distribution of energy described by the PPS went through lots of interactions that eventually created the observables we measure now.

We know the evolution from the primordial Universe is described by a system of Boltzmann equations. They can be translated into the power spectrum language as growth functions that act on the various momenta controlling how a mode grows or get damped as time pass by. As we will further develop in section 5.1 they act linearly on the smallest modes or non linearly on bigger one due to gravitational effects becoming more and more relevant.

The most straightforward way to address the problem of reconstructing the PPS given "present days" observations would be to invert the growth function. It would have been so much computationally demanding that such an approach is almost infeasible. The other way around is to try to solve the direct problem instead that the inverse one. It is easier to evolve the system many times, starting from slightly different input points, until the reconstructed Universe is the right one than to perform the inversion of the growth function. So solving a system of Boltzmann equation very fast will do the trick.

CLASS is one of the latest publicly released Boltzmann codes. Those are computer programs meant to integrate huge systems of Boltzmann equations to simulate a Universe evolution. Starting with very basic programs, such as the

pioneering COSMICS, in the years they achieved better and better results in terms of precision and speed. Every new program implemented new algorithms, optimization methods and approximation schemes. Now the current generation Boltzmann codes, CLASS and CAMB, allow to predict values accurate enough to be matched with data from precision cosmology experiments such as Planck. Either they are fast enough to be used with their ancillary Monte Carlo codes, respectively Monte Python and CosmoMC, for parameters estimation via MCMC, i.e. to be run 10,000 ∼ 100,000 times in a manageable time.

CLASS has been developed with those goals in mind and is implemented in a modular, user friendly way. The improved or never-implemented-before approximations it uses are described in [20].

For our purpose we needed to control the form of the PPS. One of the main reasons of choosing CLASS over CAMB came from this need. With CLASS there has not been needs to modify the main code as it is ready to accept an externally provided program that generates the PPS which CLASS will use. It just calls the program internally at the beginning of the run, allowing to pass up to 10 custom variables set by the user and defined in a suitable input file. Each parameter is determined by a number from 1 to 10, i.e. *custom1, ..., custom10*. My routine uses, as additional custom parameters, the values of the input PPS in the knots. It is easy, if computing power is available, to extend the precision of the present analysis that actually uses only five knots. Then the routine prints the PPS reconstructed via spline as a list of points $(k, P(k))$. This output is piped back to CLASS that uses it to calculate the observables. Notice that while the knots value is defined in run time, the knots position in k-space is hardcoded in the subroutine. When the number of knots or their position is changed to adjust for the current purpose, one has to manually modify it and to recompile the subroutine code. Having described how to compute theoretical expectations for the relevant observables (i.e. CMB and matter power spectra) using CLASS, we now have to consider the problem of fitting our models to actual data. This will be addressed in the following section.

4.4.2 Monte python and code development

At the end of the day, in order to put some constraints on the parameters we need to compare them with the real world. Monte Python (MP) is a Monte Carlo code developed specifically for cosmological parameters extraction [21]. MP is a powerful tool that takes charge of all the required processes aside Boltzmann solving. It is built to work in pairs with CLASS and act as a wrapper. The user just need to interface with Monte Python, specifying which are the fixed parameters CLASS has to use (e.g. α_p, that is set once and for all for each run), which are the parameters that have to be fitted via MCMC, and the options CLASS has to use. On top of that, as we will illustrate below, one can select data from some of the built in experiments or add his own to calculate the likelihood. Then MP

takes care of calling CLASS and run it with all the desired settings to compute the cosmological observables. Said observables are then handled by MP again that evaluates the required likelihoods. Likelihood evaluation is of course the essential ingredient which then allows MP to perform MCMC parameter estimation, using the Metropolis-Hastings algorithm, described earlier, or one of the other built in procedures. The codes already implements various techniques to optimize the algorithm settings, and at the end of the run generates an improved covariance matrix. This can be used in the input of a subsequent run so that Monte Python can reparametrize the parameter space and calibrate the step size in order to improve its efficiency. Since all of this is done autonomously, the user just has to run the program a few times just to create a good covariance matrix, and then let the chain get the required significance when he is pleased with the acceptance rate.

The penalty for the spline roughness has been added as a new likelihood package. This way it exploits the modular structure of Monte Python: it can be switched on or off when needed without needs for alter the main code. The penalty likelihood package act just like a normal likelihood package, adding to the log likelihood given by the real experiments its contribution. As said before in (4.8), it calculates the integral of the squared second derivative of the spline times a coefficient. To do so it takes as input the coefficient and the PPS value on the knots, while knots position are hardcoded in the new penalty likelihood package, as for the subroutine that calculates the PPS. It invokes again de Boor's code to recalculate the very same spline as the previously used one, and finally calculates the integral [14], which is analytic, obvious since a spline is constructed by a series of cubics. Again, when the number of knots or their position is changed one has to modify it in the code by hand. Extra care should be taken in double check that knots positions match in both pieces of code, as the program would throw no error at all for not equal position, and would print in the standard output a nonsensical analysis as if nothing wrong has happened. We acknowledge that it could be a source of errors that could have been easily solved using the custom parameters to pass both knots value and position. On the other hand it would have halved the number of "ready-to-use" knots available without major modification of the original code of both CLASS and MP. As we have done now, with just a little attention from the user, up to 10 knots are ready to use.

Chapter 5

Description of data analysis

As we have seen most of the models produce oscillatory features. In order for the spline to recover the signal if the right model had this kind of features, and actually improve the fit in comparison to a vanilla ΛCDM model, we would need to place the knots with a spacing of the same order as the wavelength. Even though this would be the optimal way to recover the signal, it would unfortunately require an enormous computational power and lots of time for the chains to run. For features with short period we would need many knots, which would translate into many parameters. Each value should be inferred via MCMC. As we said adding new parameters doesn't slow down a MCMC as much as it would with other inference methods, but there is nevertheless a limit to the largest amount of parameters that a MCMC can analyse in a feasible amount of time. Adding too many knots would require a prohibitive amount of computing time.

We found that a good compromise to obtain a resonably accurate reconstruction, while keeping computing time under control, was achieved by working with 5 knots. With this number it is almost impossible to recover the oscillatory trend of the proposed models if the frequencies are of the order of the best fit found in [8] and presented in figure 3.1. In terms of the original aim of this work, namely to test oscillatory PPS, the current analysis can be thus seen as somewhat inadequate, and not very useful. There are however several reasons why this is not really the case. First of all, the 5-knot analysis has to be seen as a necessary preliminary setup of the pipeline, that is now ready to be extended to a larger number of knots in the near future, without any further modification or additional check. Second of all, even in the current configuration, our spline reconstruction algorithm *is already able* to study several effects that, as we will see, are very interesting and smooth enough to be accessible the present resolution. Finally our choice doesn't prejudge the possibility of recovering actual features of the power spectra: it is true indeed that we lack the resolution to recover the said feature, but if, by chance, an oscillatory feature with a period big enough is there, we will still see it. On top of that the step features usually have both fast oscillation and

bigger imprints left where the inflaton crossed the step. That kind of feature could easily be recovered. If that's the case then we would know where to concentrate the analysis to do a more accurate search for oscillations later on.

5.1 Mock PPS Feature: Massive Neutrinos

The vanilla ΛCDM model assumes zero mass neutrinos. As we already pointed out it is fairly in good agreement with current data, but since considering massive neutrinos is one of the more straightforward possible extension of the ΛCDM model, cosmologists have always been interested in it. With oscillation experiments results confirming that at least two neutrino states are massive, extending the ΛCDM model was no more a speculation and became necessary. Even though particle physics experiments are really helpful in providing a lower bound on the mass sum, they are clueless about determining the absolute mass scale. One way to pin down the masses is using beta decay experiments. In the process

$$n \rightarrow p + e^- + \bar{\nu}_e \tag{5.1}$$

all the masses aside the neutrino one are known. Measuring the end-point of the electron velocity distribution one can put a constraint on the neutrino mass. The problem is that the resolution is not so high, and until now is possible to put an upper bound only a couple of order of magnitude higher than the lower bound.

In the end, relying on particle physics experiments alone one get the constraints [22]

$$0.056(0.095)\text{eV} \leq \sum m_\nu \leq 6\text{eV}. \tag{5.2}$$

Luckily, extending the ΛCDM model to massive neutrino is not just an academic exercise as cosmological data allows to put a stricter upper bound, improving the other one by at least one order of magnitude. Such a constraint do not come without caveats. Even though more or less all studies do improve the limit with respect to beta decay experiments, there is an ongoing debate in the cosmological community on how to interpret some tensions between measurements coming from different datasets. The topic is of particular importance because it has been linked to a more general tension between CMB and local measurements of various cosmological parameters. In particular we are referring to H_0 and σ_8. The Hubble parameter has been measured extrapolating up to today the best fit of the *Planck* CMB power spectra [23] and with Hubble telescope redshift measurements [24]. The two estimates differs by 2.5σ. σ_8 is the r.m.s. mass fluctuations in spheres of 8 Mpc$/h$ at the present epoch and is a parametrization of the clustering amplitude. It is not directly measured in CMB power spectra nor in galaxies catalogue but it can be calculated from other measured parameters. If inferring it from CMB data give the value $\sigma_8 = 0.8233 \pm 0.0097$ [23], local measurement fluctuate around the value $\sigma_8 = 0.77 \pm 0,02$ [25].

Many recent studies combined analyses of multiple datasets to conclude that some expansions in the neutrino sector of the ΛCDM model could help solve the problem. Changes in the number of families, addiction of sterile neutrinos, different sums of the masses and numbers of relativistic species have been all considered as possible solutions of the tension on H_0 [26], σ_8 [27, 28, 29, 30, 31] and a potential tension between *Planck* and BICEP [32] constraints on $r_{0.002}$, the tensor-to-scalar ratio at $k = 0.002$ Mpc^{-1} (that was however solved when reanalyzing BICEP data with accurate polarized dust templates from Planck). Other works rejects those conclusions, favouring model with no sterile neutrinos and lower masses [23, 33, 34, 35, 36, 37].

With our PPS reconstruction we will be able to put a constraint on neutrino mass. Since the statistical analysis we carry on is very solid we hope this work will help to settle the debate. But first we need to show what is the relevance of neutrino masses in cosmology and what is their peculiar imprint on the power spectrum.

We will work in the longitudinal gauge, which requires vanishing non diagonal elements of the metric. We will be only interested in scalar perturbations so, since at first order scalar, vector, and tensor perturbations decouple, we can omit all perturbation parameters except for the scalars [7]. The perturbed metric becomes

$$ds^2 = g_{\mu\nu}dx^\mu dx^\nu = a^2(\tau)[(1 + 2\phi)d\tau^2 - (2\psi)\delta_{ij}dx^i dx^j]. \tag{5.3}$$

The four scalar degrees of freedom can be identified in the perturbed energy-momentum tensor as

$$\delta T_0^0 = \delta\rho, \tag{5.4}$$

$$\delta T_i^0 = (\bar\rho + \bar p)v_i^\parallel, \tag{5.5}$$

$$\delta T_j^i = -\delta p\,\delta_j^i + \Sigma_j^{i\,\parallel}, \tag{5.6}$$

where $v_i^\parallel$ is the longitudinal component of the velocity field, and $\Sigma_j^{i\,\parallel}$ is the traceless longitudinal-divergence component of the momentum tensor δT_j^i. Each of them can of course be parametrized with a scalar field such as

$$v_i^\parallel = \partial_i\tilde v, \tag{5.7}$$

$$\Sigma_j^{i\,\parallel} = (\partial^i\partial_j - \frac{1}{3}\delta_{ij}\nabla^2)\tilde\sigma, \tag{5.8}$$

or using the velocity divergence θ and the shear stress σ

$$\theta = \sum_i \partial_i v_i = \nabla^2\tilde v \tag{5.9}$$

$$(\bar\rho + \bar p)\nabla^2\sigma = -\sum_{i,j}(\partial^i\partial_j - \frac{1}{3}\delta_{ij}\nabla^2)\Sigma_j^{i\,\parallel} = -\frac{2}{3}\nabla^4\tilde\sigma. \tag{5.10}$$

As everything has been carefully parametrized, we can plug those expressions in the perturbed Einstein equations

$$\delta G_{\mu\nu} = \delta R_{\mu\nu} - \frac{1}{2}g_{\mu\nu}\delta R = 8\pi G\delta T_{\mu\nu}. \tag{5.11}$$

where $\delta R_{\mu\nu}$ and δR are the Ricci tensor and scalar built with the perturbed metric. Bianchi identity

$$\delta R_{\alpha\beta[\mu\nu;\rho]} = 0 \tag{5.12}$$

guarantees that the LHS of Einstein's equation is covariant conserved, so the energy-momentum tensor is too. By imposing it one get the continuity equation

$$\dot{\delta} = (1 + w)(\theta + 3\dot{\psi}), \tag{5.13}$$

where we introduced the state parameter $w = \bar{p}/\bar{\rho}$, and the fractional overdensity field $\delta = \delta\rho/\bar{\rho}$, and the Euler equation

$$\dot{\theta} = \frac{\dot{a}}{a}(3w - 1)\theta - \frac{\dot{w}}{1 + w}\theta - k^2\phi - k^2\sigma - \frac{w}{1 + w}k^2\delta. \tag{5.14}$$

Those two relations are exact so they can be evaluated at any time. We are interested in cold dark matter. It is well described by a collisionless fluid, which has $w = 0$, and the shear stress can be neglected $\sigma = 0$. Under those two assumptions, plug Eq. (5.13) into Eq. (5.14) gives

$$\ddot{\delta}_{cdm} + \frac{\dot{a}}{a}\dot{\delta}_{cdm} = -k^2\phi + 3(\ddot{\psi} + \frac{\dot{a}}{a}\dot{\psi}). \tag{5.15}$$

Now we need a couple more relations. From the off-diagonal spatial-spatial component of the Einstein equation we get

$$\delta G_j^i = a^{-2}\left(\partial^i\partial_j - \frac{1}{3}\nabla^2\delta_j^i\right)(\phi - \psi) = 4\pi G\delta T_j^i \quad i \neq j \tag{5.16}$$

$$k^2(\phi - \psi) = 12\pi Ga^2(\bar{\rho} + \bar{p})\sigma. \tag{5.17}$$

From this last equation we evince that if σ vanishes the difference between ϕ and ψ is negligible. Then we need the Poisson equation for the gravitational potential in the Fourier space

$$-\frac{k^2}{a^2}\psi = 4\pi G\delta\rho. \tag{5.18}$$

We can go back to the RHS of Eq. (5.15). Deep inside the Hubble radius the comoving gradient $-k^2\phi$ dominates the source term. In the absence of shear it can be approximate by $-k^2\psi$, and finally using the Poisson equation we get

$$\ddot{\delta}_{cdm} + \frac{\dot{a}}{a}\dot{\delta}_{cdm} = 4\pi G \ a^2 \ \delta\rho \tag{5.19}$$

where $\delta\rho$ is the total density perturbation.

We are now ready to show how the neutrino mass affects the evolution. We are considering scales $k \gg k_{nr}$ where k_{nr} is the scale at which the neutrino became non relativistic. This way the fact that neutrino are massive or not does not affect the Poisson equation we used earlier (Eq. (5.18)). Nevertheless, neutrino background affects the expansion rate. The first Friedmann equation Eq. (2.4) is

$$\frac{\dot{a}^2}{a^2} = \frac{8\pi G}{3}(\rho_{\rm cdm} + \rho_{\rm b} + \rho_\nu) \tag{5.20}$$

where $\rho_{\rm b}$ is the baryon energy density and ρ_ν is the neutrino energy density. Even though there could be both massive and massless neutrino, it is a safe assumption that ρ_ν is dominated by the massive ones, so it decays just like other energy densities during matter domination, like a^{-3} [22]. Then we know that the quantity

$$f_\nu = \frac{\rho_\nu}{\rho_{\rm cdm} + \rho_{\rm b} + \rho_\nu} \tag{5.21}$$

is approximately a constant.

Solving Eq. (5.20) for $\rho \propto a^{-3}$ we get $a(t) \propto t^{2/3}$, and by definition of conformal time $d\tau = a^{-1}dt$, we obtain $a \propto \tau^2$. Then Eq. (5.19) is (cf. Ref. [22])

$$\ddot{\delta}_{\rm cdm} + \frac{2}{\tau}\dot{\delta}_{\rm cdm} - \frac{6}{\tau^2}(1 - f_\nu)\delta_{\rm cdm} = 0. \tag{5.22}$$

This can be easily solved with the ansatz $\delta_{cdm} \propto \tau^{2p}$: one finds two roots for p

$$p = \frac{-1 \pm \sqrt{1 + 24(1 - f_\nu)}}{4} \tag{5.23}$$

We are interested in the growing solution, so expanding at first order in f_nu, since $a \propto \tau^2$, we get the result

$$\delta_{\rm cdm} \propto a^p \approx a^{1 - \frac{3}{5}f_\nu}. \tag{5.24}$$

During the matter domination, for scales bigger than the one typical of neutrino relativistic-non relativistic transition, the growth of cold dark matter perturbation is damped by the presence of massive neutrino, as described in Eq. (5.24). This in turn, has the observable effect of damping the matter power spectrum amplitude on those scales.

We note that our data analysis will not be restricted to the region in which our previous discussion holds. It is possible to generalize the previous results, but only in a semi-analytical way, that requires comparison with numerical simulations. Since it would be not so interesting, we present here only a numerical reconstruction of the effect that massive neutrinos have on the matter power spectrum.

In figure 5.1 we explicitly show how considering neutrino masses affects the matter power spectrum (mPk). Using the code CLASS we generate two mPk.
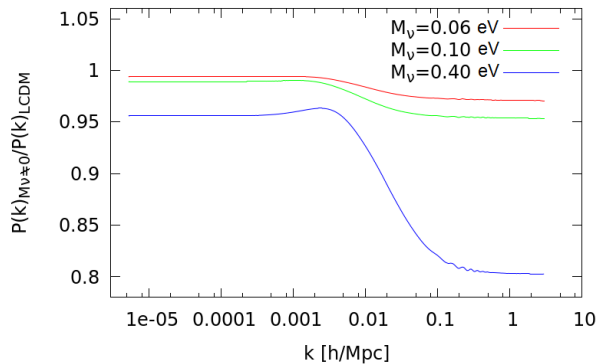
Figure 5.1: Ratio of theoretical predicted matter power spectra with 3 massive neutrinos divided by the vanilla ΛCDM matter power spectra. The mass value in the label refers to the sum of the mass of the considered neutrino. All the neutrinos are non degenerate, the mass splitting is known thanks to oscillation experiments.

The first is the matter power spectrum of a vanilla ΛCDM model with 3 massless neutrinos plus the best fit cosmological parameters of the experiment *Planck* (ref. [23]) that will be described shortly. The second has been evaluated with the very same parameters but with three massive, non-degenerate, neutrinos. We used the mass splitting known from oscillation experiments [38]. In figure the "massive neutrino mPk" has been divided k per k by the "massless neutrino mPk" to show the damping effect for various sums of the masses. As we expected, all mPk have the same normalization at small k, then after crossing the free streaming length the mPk is damped more and more as the mass sum increase.

Everything we said up to now applies to the matter power spectrum and not to the PPS which is in principle not affected. Even though we reconstruct the primordial power spectrum, we are however still sensitive to neutrino masses, as their presence would distort our reconstruction due to the linearity of the growth functions [39].

To clarify this concept it is better to stick to an example to fix the idea. Figure 5.2a – fig. 5.2e should help visualize the explanation. We repeat that for the argument to work we have to consider only scales where evolution is linear, i.e. $k < 0.2 \ h/$Mpc. Consider a universe with a ΛCDM model and massive neutrinos, all the cosmological parameters are known. At the end of inflation, the PPS was a perfect power law (figure 5.2a). Starting from the known initial condition we can evolve the system. In doing that we shall remember to consider the neutrino masses in the evolution equations. As we know their effect is a damping at high k (figure 5.2c). We would end up with a certain matter power spectrum (figure 5.2e), and a full set of all the other possible observables, that we are not interested in. Now we can think of another procedure. Since we know the effect of massive neutrinos (figure 5.2b), we could multiply the damping k per k to the power
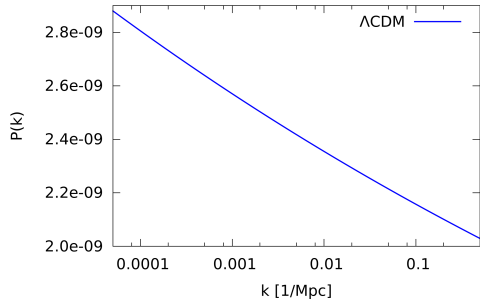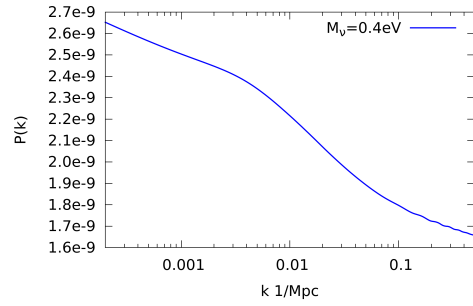
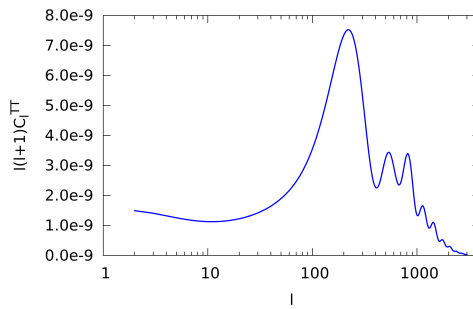(a) In the first case the initial condition is a power law PPS.
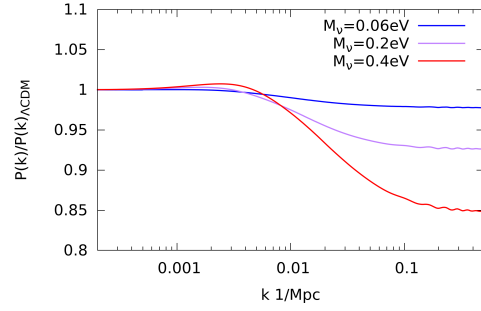
(b) In the second case the neutrino damping is considered in the initial conditions.
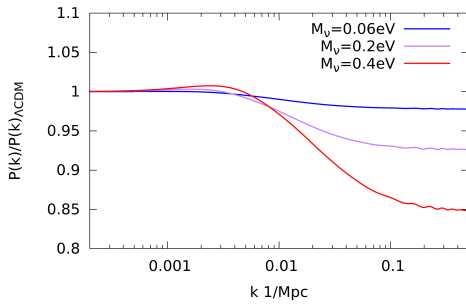
(c) Then the evolution takes into account the presence of massive neutrino.

(d) The initial condition is a power law multiplied k per k to the neutrino damping. Then the evolution equation with massless neutrino is used.

(e) The two methods generate the same observables in the scales of interest. Here a CMB power spectrum, but the same applies to the mPk.

law PPS we had in the beginning. We would obtain a power spectrum slightly different from a power law, as it has a very smooth damp feature (fig. 5.2d). Now we can use the damped spectrum as initial condition and apply the known evolution equation with massless neutrino. In practice in this second scenario we apply the neutrino damping not in the evolution but in the initial condition, and then of course we do not re-apply it again. The linearity of the evolution equation guarantees that the generated matter power spectrum would be exactly the same of the first case (figure 5.2e).

What we are going to do then is to set CLASS so that in the Monte Carlo Markov Chains neutrino are not considered. If there were detectable massive neutrinos in the real data, we would recover the damp feature in the primordial power spectrum, just as we explained in the second scenario.

Now we have to do some very important remarks.

- Let us stress again that we are not saying that the mass of neutrino has a direct effect on the primordial power spectrum. Normalization and shape of the PPS depend only on characteristics of the inflation (or whatever other model that could replace inflation). Neutrino mass affects only the evolution of perturbations at later times. If we see the signal on the PPS is only thanks to linearity and the fact we have voluntarily omitted their influence on transfer functions.

- In the case we should see a signal such as that shown in figure 5.1 we can not infer that it is just due to neutrino masses. Other particles beyond the standard model could easily share the same properties of neutrinos when it comes to damping perturbations. But if we were to impose an upper bound θ then we can be sure that

$$\theta > \sum_\nu m_\nu + \sum_X m_X > \sum_\nu m_\nu \qquad (5.25)$$

  where X are the other possible particles. So the upper bound would hold even for neutrinos alone.

- In our analysis the damping is completely degenerate with the shape of the PPS. For example we would not distinguish a vanilla ΛCDM universe from a universe with massive neutrinos plus a PPS with enhanced power at high k that exactly cancel the neutrino damping. So to be rigorous we can not impose an upper bound to neutrino masses in general, but we can impose it if we assume that the ΛCDM model is correct, or if we assume that it deviates less than the bound accuracy.

To be sure that our reconstruction is accurate enough to be sensitive to the damp we have tried to recover a known signal. We multiplied the damping ratio generated with CLASS of figure 5.1 to a power law signal. Then we tried to
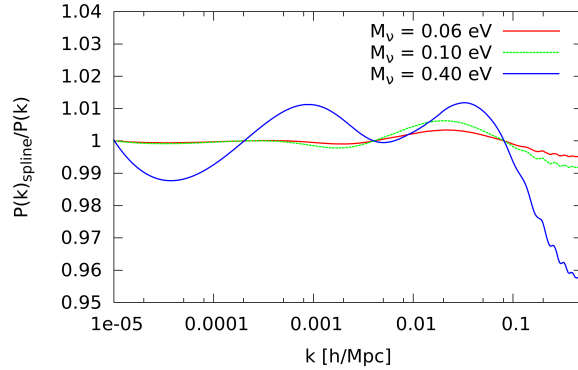
Figure 5.3: a

$\sum m_\nu$	maximum damping	maximum error
0.06 eV	3%	0.5%
0.1 eV	5%	0.8%
0.4 eV	20%	4%

Table 5.1: Cross-validation datasets CV_A and CV_B for the various runs.

use a spline to reconstruct it and we checked the difference. As it came out we
have errors much smaller than the effect of the damping. Figure 5.3 shows the
ratio of the spline reconstruction to the signal for various neutrino masses. By
comparing it with figure 5.1 we can obtain the data shown in table 5.1. As shown
the error of the reconstruction is always less than one fifth of the signal. After
this preliminary test, we are thus confident that we are able to retrieve a neutrino
damping signal, if present in the data and if the value of the mass is high enough.
In fact here we have quantified only the error due to the use of the spline, and
not the errors due to the fit procedure. Those will be know once the likelihood
distribution is known. A discussion about errors is carried when the results are
shown in the chapter 6.

5.2 Analysed Datasets

In the present work we use cosmic microwave background radiation data from
Planck and WMAP, and the determination of the matter power spectrum from
four experiments. Planck and The Canada-France-Hawaii Lensing Survey use a
weak lensing technique while WiggleZ and SDSS uses galaxy maps to measure the
matter power spectrum. We tried to incorporate in our work all the most recent
experiments that could give constraints on the shape of the PPS. In figure 5.4 we
show the scales probed by each experiment. In the following we briefly describe
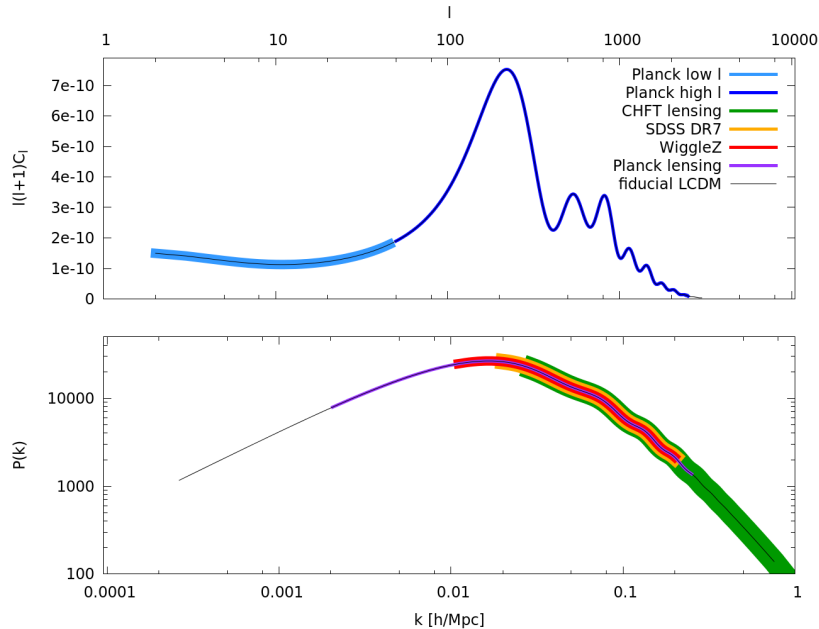
Figure 5.4: Scales covered by the experiments used in our analysis

them and list the specific datasets we use.

5.2.1 CMB Temperature and Polarization Data

Planck is an ESA satellite dedicated to the study of the early Universe and of its evolution [40]. Launched on 14 May 2009 in the L_2 Lagrangian point, it has continuously recorded data from 12 August 2009 to 23 of October 2013.

The main goal of the experiment is to measure the temperature anisotropies of the cosmic microwave background (CMB). Its design was conceived to have an instrumental precision such that the measures accuracy is basically limited by fundamental astrophysical effects (in the range $0 < \ell < 2000$). The second goal of the mission is to measure to high accuracy the CMB polarization anisotropies, providing both increased precision in the determination of cosmological parameters and a further probe of Early Universe physics. It is worth mentioning that as a side effect of its need to determine as best as it can the foreground, in order to remove it, *Planck* offers lot of information on properties of extragalactic sources and a map of dust and gas in the intergalactic medium.

The satellite was equipped with array of 74 detectors sensitive to frequencies between 30 and 857 GHz, which scanned the sky with angular resolution between 33' and 5'.

Planck mapped the whole sky twice a year reaching a combination of sensitivity, angular resolution, and frequency coverage never achieved before.

Since we want to fit both the PPS value at the knots and the cosmological parameters Ω_{CDM}, Ω_b, h, and τ_{reio}, it is mandatory to use in every run *Planck* data on temperature and polarization anisotropies [39]. Since a relatively higher baryon density Ω_b enhances odd CMB power spectrum peaks in respect with even peaks, it can be inferred from the ratio between the first and the second peaks. For a fixed baryon density, a higher dark matter density increases the total non-relativistic matter content of the Universe. So an increment of Ω_{cdm} suppresses radiation driving, decreasing the overall amplitude of the peaks, and the the value of the parameter could be inferred from first peak to third peak ratio. Once the other densities are fixed, h can be used to parametrize the total energy density, and its effect manifests as a shift of the whole power spectrum towards higher or lower ℓ. Finally τ_{reio} act as a damping over anisotropies on smaller scales, and it shrink the power spectrum amplitude. Since it is exactly the same effect that multiplying the PPS for a constant has, it is impossible to break the degeneracy between τ_{reio} and a shift in all the knots value with a temperature measure only. Here polarization comes into play, because rescattering of photons after reionization generate a polarization signal at low-l which helps breaking the above mentioned degeneracy.

The *Planck* collaboration released in 2013 the temperature data from the first half of the mission [41]. In 15.5 months of data-taking period the satellite completed 2.6 surveys of the sky. Temperature data come in two sets:

- **Commander** TT, TE, EE two point correlation function data from $\ell = 2$ to $\ell = 49$,

- **CamSpec** TT data from $\ell = 50$ and up to $\ell = 2500$

Polarization data has not be released until June 2015, so it has been available only for the final run. Since they are needed to constrain τ_{reio} we use the final WMAP polarization data release in tandem with *Planck* temperature [42]:

- **lowlike** TE, EE, BB data up to $\ell = 32$ from the WMAP experiment.

5.2.2 Planck lensing

Beside the CMB power spectrum, *Planck* reconstructed the CMB lensing potential [43], which contains information on the amplitude of large scale structure integrated from recombination up to present time. Such data are inferred from the study of the four point function of temperature anisotropies (in 2015, both temperature and polarization are included). We will refer to it as PlanckLens

All *Planck* and WMAP likelihoods are managed by the official *Planck* collaboration release, Clik.

5.2.3   CHFTLenS

The Canada-France-Hawaii Lensing Survey, hereafter referred to as CFHTLenS uses data collected between mid 2003 and early 2009 within the CFHT Legacy Survey at the CHF observatory on Mauna Kea, Hawaii [44]. The CFHTLenS survey analysis combined weak lensing data processing with THELI [45], shear measurement with lensfit [46], and photometric redshift measurement with PSF-matched photometry [47]. A full systematic error analysis of the shear measurements in combination with the photometric redshifts is presented in [48], with additional error analyses of the photometric redshift measurements presented in [49]. To be specific, we make use of the tomographic weak lensing signal to constrain the shape of the power spectrum. The collaboration released the likelihood evaluator code for COSMO MC only, while MP was not supported. The ICC-UB group, with major contribution from A. J. Cuesta, has implemented it into MP and released the code.[1]

5.2.4   WiggleZ

The WiggleZ Dark Energy Survey has been a large scale galaxy survey carried out over 276 nights from August 2006 and January 2011. Measurements were taken at the Anglo-Australian Telescope in Siding Spring Mountain, near the New South Wales town of Coonabarabran, Australia. The primary objective of WiggleZ was to detect the BAO scale at higher redshifts than was possible before it. Through position and redshift measurements of 238,000 galaxies it mapped a volume of one cubic Gigaparsec in seven regions of the sky up to a redshift equal to one. The information stored in those maps was then converted in a matter power spectrum [50]. To do so galaxies were divided in 4 subgroups with different redshift in order to be analysed separately. All the galaxies in a given redshift bin were given an effective redshift. This way the momentum dependence of the power spectrum for each bin could be inferred with a simple angular measurement. The constraints coming from the four power spectra at different redshift are released by the WiggleZ collaboration and have been incorporated in MP and released with the code

5.2.5   SDSS DR7

The Sloan Digital Sky Survey used its 2.5 m telescope based in the Apache Point Observatory, New Mexico, to collect 929,555 galaxy spectra. In data release 7, the collaboration used a sample of luminous red galaxies to reconstruct the halo density field and its power spectrum roughly between $k = 0.02h/\text{Mpc}$ and $k = 0.2h/\text{Mpc}$ [3]. The collaboration released the likelihood evaluator code for

---

[1]It is available at `https://github.com/ajcuesta/montepython_public/tree/CFHTLens_correlation`

COSMO MC only, while MP was not supported. The ICC-UB group, with major contribution from A. J. Cuesta, has developed the version for MP used in this work.

5.3 Cross-validation setup

Cross-validation, as described in section 4.3, could have been implemented in various ways. As we already pointed out there, we decided to include each dataset as a whole in each cross-validation set, which means all data-points from one experiment were never split in CV_A and CV_B, but they were put in CV_A only or in CV_B only. The explanation of this choice is twofold. Every experiment collaboration release its own likelihood evaluator with all available data from that experiment. Using it in one cross-validation set as it comes out of the box means that there are no unaccounted errors. In fact splitting data from the same dataset in the two cross-validation set without investigating how each data is correlated with others, could introduce some difficult-to-deal-with correlations or systematics between the two CV sets. Besides that, there is the risk of introducing bugs in the likelihood codes while modifying it. Given that most of the likelihood codes we had to deal with were quite complex, *Planck* "click" above all, such a scenario would not be unlikely at all. On the other hand, confronting different experiments in the cross-validation means that we have more control on the relations between experiments and whether they all agree.

We tried to set up the cross-validation in the most symmetrical way that was possible. As we said, since we want to constrain both the shape of the PPS and the cosmological parameters, we necessarily add *Planck* temperature power spectrum and WMAP polarization power spectra to all runs. We will refer to them as the CMB experiments. Besides these, we have 4 other experiments: 2 that use weak lensing and 2 using galaxies catalogues. We will refer to them as the matter power spectrum (mPk) experiments.

We have done 3 runs in a pyramidal scheme. We start performing in parallel two different cross-validation analysis on two couples of experiments. Each couple is formed by a weak lensing experiment and by a galaxy catalogue. Therefore for each couple one experiment is in CV_A and the other in CV_B. If there are no problems at this stage the analysis is carried on. The two experiments of one couple are used in the same cross-validation set, and the other couple goes in the other one. Cross-validation is performed among the two couples. Once we find the best value for the penalty weight, we are able to perform the final run of the MCMC that will lead to our reconstruction. This final run is performed using all the experiments together and the penalty set at its optimal value.

The composition of each run, and the tag that will be used in the following to refer to it, are shown in table table 5.2.

Once the set up has been chosen, we had to find the minimum of the CV score

Run	CV_A	CV_B
1.1	CMB, PlanckLens	CMB, SDSS DR7
1.2	CMB, CFHTLenS	CMB, WiggleZ
2	CMB, PlanckLens, SDSS DR7	CMB, CFHTLenS, WiggleZ

Table 5.2: Cross-validation datasets CV_A and CV_B for the various runs. With "CMB" we refer to CMB temperature and polarization data from *Planck* and WMAP.
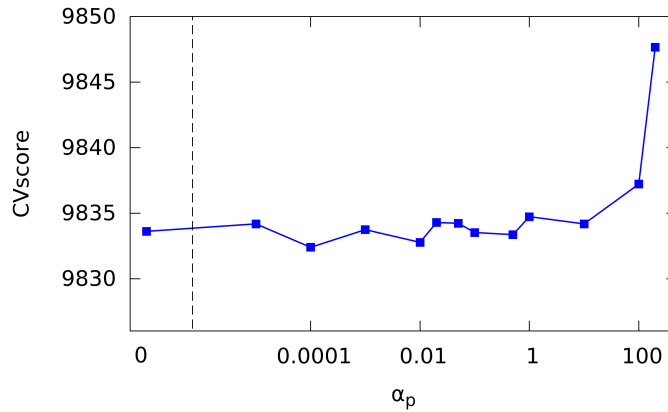

Figure 5.5: CV score as a function of α_p for the Cross Validation run 1.1

to determine the optimal value of the penalty weight α_p. We recall that to find the CV score for a given α_p one has to calculate the logarithm of the likelihood of CV_A given the CV_B best fit plus the other way around, swapping A and B.

The procedure to find the CV score for a fixed α_p was the following. A MCMC was run with the likelihoods of CV_A experiments plus the penalty, while another one was run with the likelihoods of the CV_B experiments, plus the penalty again. Once both of them converged the two posteriors were known and so were the two best fit. Those were used to calculate the CV score for a defined α_p.

To find the minimum we sampled the CV score repeating this process many times for different α_p. Since we found that the minimum is not so sharp and well defined, we decided to not automatize the sampling, for example by choosing points from a grid. Even though we started sampling using equally spaced α_p in log space, we took more points whenever necessary.

In figure 5.5 we show the cross-validation score for the run 1.1, which compares *Planck* Lensing with SDSS DR7. As CMB temperature and polarization data from *Planck* and WMAP are common to every run we will assume their presence, without explicitly specifying it, for each run from now on. The CV score has a fairly well defined wall on high penalty weight, but is quite constant under a certain threshold, say $\alpha_p = 10$. For high α_p the penalty would be the only relevant
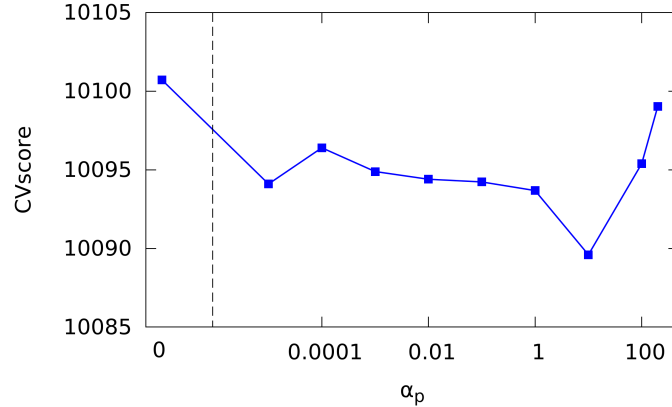
Figure 5.6: *CV* score as a function of α_p for the Cross Validation run 1.2

contribution to the likelihood, so it is obvious that the *CV* score grows fast as α_p grows. On the other hand the explanation of the behaviour at small weight is less clear, and there is room for interpretations. As we said in section 4.1 we put two extra false knots at each end of the spline to be sure it would behave well allowing the MCMC to converge fast enough. Probably this guarantees that the spline cannot assume a too-unlikely shape even if the weight is low. The other possibility, which probably acts in partnership with the first, is that we have many measures with a very high accuracy which are apparently quite consistent among themselves. This again means that data themselves disfavour unnecessarily wiggly shapes, even when there is a low penalty.

For run 1.2, WiggleZ vs CFHTLenS, the CV score shown in figure 5.6 is pretty similar. The first notable differences is lower CV score for high penalties. The second is a little increase for $\alpha_p \to 0$ as we initially expected, but as the CV score merely increases of a few units, we are confident it has no strong statistical relevance. It is however a hint that the spline need to be at least a little bit constrained.

Since, aside from a not well defined boundary about how low the penalty should be, the preliminary runs do not highlight any problem, we carried on with run 2, which involves all experiments. The CV score is shown in figure 5.7. This again resembles a lot the CV score from run 1.1, with a sharp increment for α_p that goes from 100 to 200 and oscillations around a mean value for lower penalties.

Since we had to deal with this scenario, with a not well defined minimum, we have decided to present two different results. One is more conservative, in the sense that it has a stronger penalty that allows only small deviations from the concordance power law model. For this one we choose $\alpha_p = 1$. The other leaves more freedom to the data, as we choose a more relaxed penalty $\alpha_p = 0.01$. It could appear as a small variation from the conservative analysis, but we have to
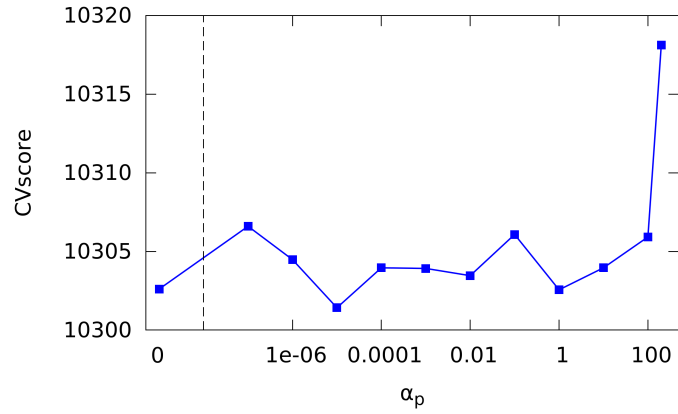
Figure 5.7: CV score as a function of α_p for the Cross Validation run 2

think about convergence time and errors. More freedom translate not only into wigglier lines but also into enhanced uncertainties. Since reconstructions from run 1.1 and 1.2 coincide with the cross-validation sets for run 2, analyse the low-α_p runs requires no additional work. However it is pretty much uninformative, as errors are, for some parameters, even more than one order of magnitude larger than the best fit.

Chapter 6

Results

We recall that the free parameters in our MCMC runs were the mean baryon density ω_b, the cold dark matter density ω_{cdm}, the rescaled Hubble parameter h, the optical depth at reionization τ_{reio}, and the value on the five knots of the spline, that we used to parametrize the shape of the PPS.

We made two runs with the latest *Planck* likelihood (2015 release [51]) and all the matter power spectrum data (Planck Lensing 2015, WiggleZ [50], CFHTLenS [44], and SDSS DR7 [3]), with two different roughness penalties. The first, with a penalty $\alpha_p = 1$, is our more conservative reconstruction, as the stiffer spline allows for smaller deviation from a power law. Its best fit results, and all the relevant quantities about its parameter likelihood are presented in table 6.1.

The second run, with a penalty $\alpha_p = 0.01$ allows the splines to explore greater deviations from a power law, at the price of greater uncertainties. Its results are presented in table 6.2.

We also show the correlations between parameters in the triangular plots in figure 6.1 and 6.2. As one could have expected the values of the knots are fairly correlated. Since varying even just one knot modifies the shape of the whole spline, it seems reasonable that all knots have to work in tandem to maximise the likelihood. And that explains the correlation. The second biggest correlation is among τ_{reio} and the knots at higher k. The effect of τ on the matter power spectrum is negligible, while it cuts power to high multipole in the CMB power spectrum [22, 4, 39]. So if we focus on smaller scales and *Planck* data only the effect of τ and a damping in the PPS are degenerate. Probably *Planck* polarization data and matter power spectrum data are not significant enough to completely break the degeneracy, fact that results in the high correlation.

Now for the sake of clarity we will show the reconstructed power spectra, for both the penalty values, a few times using different quantities. We will start from the PPS itself, then it will renormalised by dividing it k per k by the *Planck* parametric power-law reconstruction. Finally we will write the PPS as if all the dependence on the scale is enclosed in a running power law index, and we will

Param	best fit	mean$\pm\sigma$	95% lower	95% upper
$100\ \omega_b$	2.232	$2.248^{+0.014}_{-0.014}$	2.221	2.276
ω_{cdm}	0.1171	$0.1166^{+0.001}_{-0.00093}$	0.1146	0.1185
h	0.6903	$0.6927^{+0.0044}_{-0.0047}$	0.6837	0.7018
τ_{reio}	0.05222	$0.05793^{+0.0083}_{-0.013}$	0.04	0.07679
10^9 knot 1	2.697	$2.643^{+0.11}_{-0.11}$	2.418	2.867
10^9 knot 2	2.479	$2.466^{+0.067}_{-0.07}$	2.33	2.602
10^9 knot 3	2.261	$2.276^{+0.04}_{-0.047}$	2.193	2.364
10^9 knot 4	2.063	$2.09^{+0.033}_{-0.05}$	2.015	2.171
10^9 knot 5	1.861	$1.898^{+0.042}_{-0.056}$	1.805	1.996

$-\ln\mathcal{L}_{\min} = 6965.45$, minimum $\chi^2 = 1.393e + 04$

Table 6.1: Best fit, mean and confidence intervals for the parameters in run 2 with $\alpha_p = 1$

Param	best fit	mean$\pm\sigma$	95% lower	95% upper
$100\ \omega_b$	2.26	$2.253^{+0.015}_{-0.015}$	2.223	2.283
ω_{cdm}	0.116	$0.1165^{+0.0011}_{-0.001}$	0.1144	0.1186
h	0.6964	$0.6936^{+0.0046}_{-0.0052}$	0.6839	0.7035
τ_{reio}	0.06336	$0.06085^{+0.0097}_{-0.014}$	0.04	0.08178
10^9 knot 1	2.512	$2.552^{+0.62}_{-0.66}$	1.325	3.767
10^9 knot 2	2.366	$2.409^{+0.27}_{-0.29}$	1.865	2.955
10^9 knot 3	2.252	$2.257^{+0.055}_{-0.059}$	2.147	2.371
10^9 knot 4	2.11	$2.104^{+0.038}_{-0.056}$	2.018	2.195
10^9 knot 5	1.881	$1.876^{+0.07}_{-0.077}$	1.733	2.023

$-\ln\mathcal{L}_{\min} = 6964.25$, minimum $\chi^2 = 1.393e + 04$

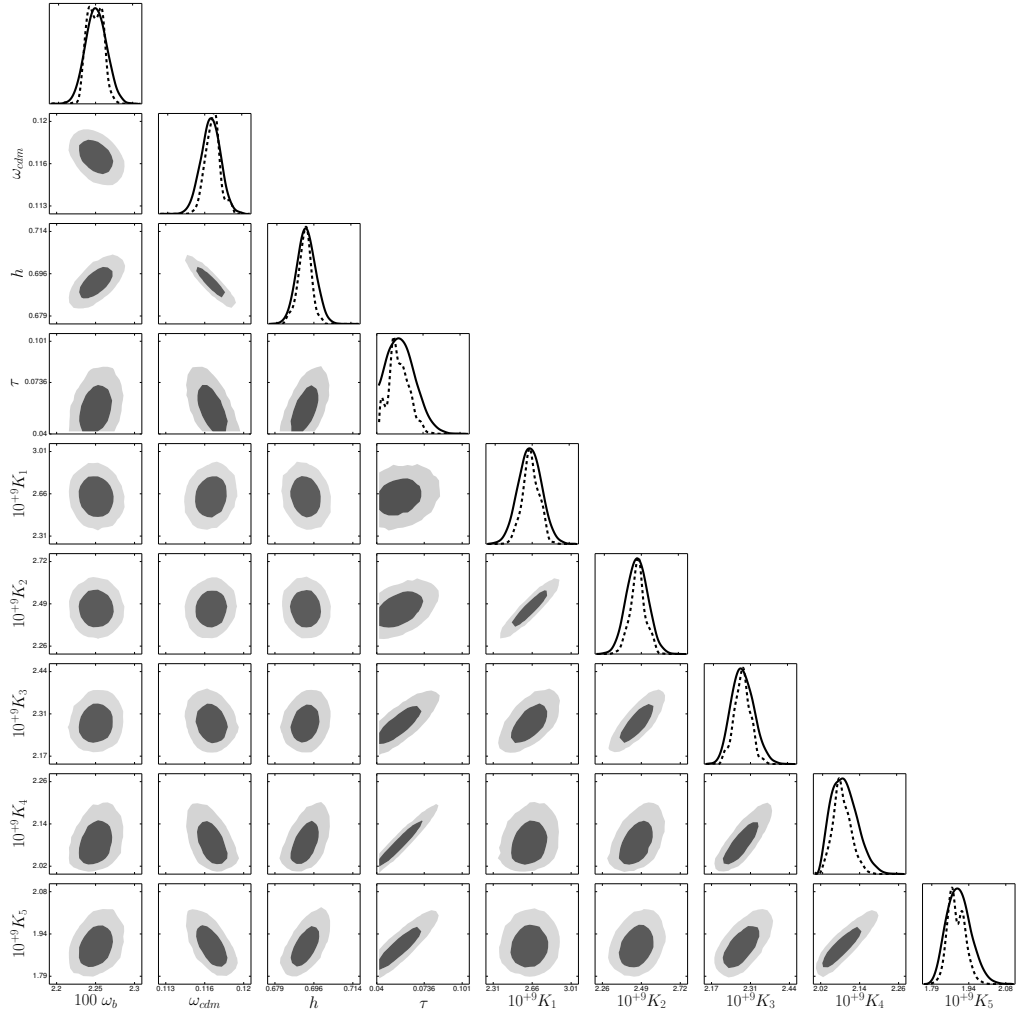Table 6.2: Best fit, mean and confidence intervals for the parameters in run 2 with $\alpha_p = 0.01$

Figure 6.1: Triangular plot for the final run with $\alpha_p = 1$. We refer to the value of the i-th knot with the label K_i.

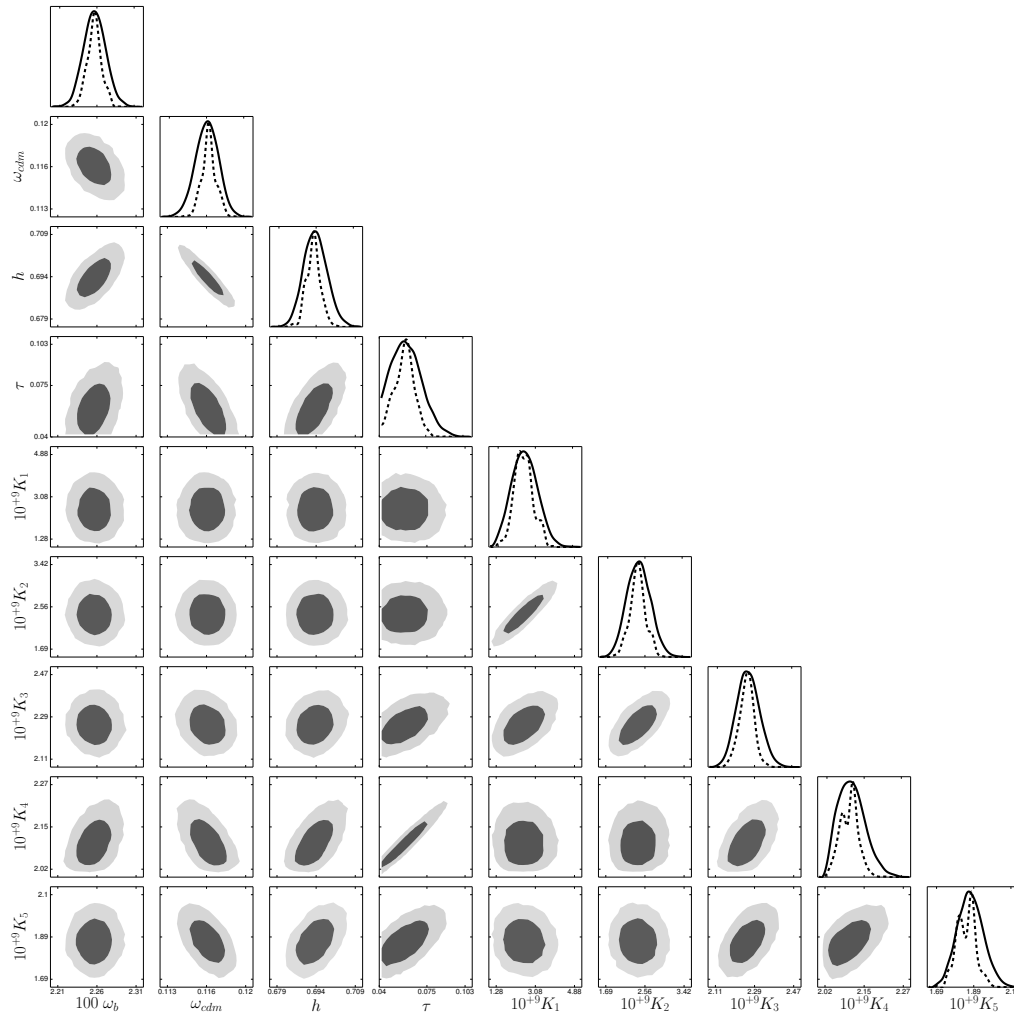Figure 6.2: Triangular plot for for the final run with $\alpha_p = 0.01$. We refer to the value of the i-th knot with the label K_i.

plot the index itself. The information enclosed in the various plot is eventually the same, but we will highlight from time to time different aspects that are easier to see from that point of view.

In figure 6.3a and 6.3b we show the reconstructed PPS for respectively $\alpha_p = 1$ and $\alpha_p = 0.01$. In the figure the red (pale red) region shows the $\pm 1\sigma$ ($\pm 2\sigma$) contour for *Planck* TT, TE, EE + Low P [1]. The black triangles on the bottom show the positions of the knots (some are not visible on the shown scales). The coloured lines on the upper side show the scales probed by each experiment as in figure 5.4, green for *Planck* lensing, lilac for WiggleZ, gold for SDSS DR7, burgundy for CFHTLenS. *Planck* CMB temperature spectrum covers the whole plot. To deal with errors we couldn't just show confidence intervals around each knot. In fact we cannot assume that splines run in an orderly manner from knot to knot: usually they do not differ only for an offset but also in shape. Consider two spline A and B that are almost equally likely, i.e. that share a similar value of $\log \mathcal{L}$ in the MCMC. This requirement do not imply that for example one spline is equal to the other plus a small constant, $A(k) = B(k) + \epsilon$, or that if A is bigger than B on one knot than it should be bigger on every knot, or other possible conditions. It is entirely possible that if A evaluated on a knot is a little bit bigger than B on the same knot, then it is very much smaller than B on the subsequent knot and finally it becomes again bigger on a third knot. To consistently show how different shapes and normalizations links to errors we sorted the points in the chains from the most likely, i.e. the best fit, to the less likely. Then we divided them in ranges: a first range that covers the 68.27% most likely points, a second range that covers points from 68.27% to 95.45% most likely and so on. As obvious we choose those percentages because if the distribution had been Gaussian they would refer to 1σ and 2σ intervals. To keep the figures not too busy we sampled 400 splines from each likelihood range and plotted them in different colours, dark blue for the most likely, and light blue for the second range. We point out that in practice splines of the two range spread on the same "distance" from the best fit. This is because more unlikely splines do not have a bigger offset in respect to the best fit. Instead they just become more and more wigglier.

The first point about the reconstruction we want to highlight is that, at least for the more conservative choice of the penalty, errors are comparable with errors from *Planck* parametric fit, that is the most accurate available. As we already pointed out, it is not to be taken for granted in a minimally parametric reconstruction, and it is one of the biggest achievements of our analysis.

Then we note how the added degrees of freedom in the $\alpha_p = 0.01$ reconstruction are used to fit a damp at low momenta. This is due to the low multipole "anomaly" of CMB power spectrum, as CMB temperature power spectrum theoretical predictions on the biggest angular scale seem to be a bit lower in power then the measurements [41].

Aside the low-multipole damp, we have not found any statistically significant feature in the PPS. Our reconstruction appear to be very smooth, with no
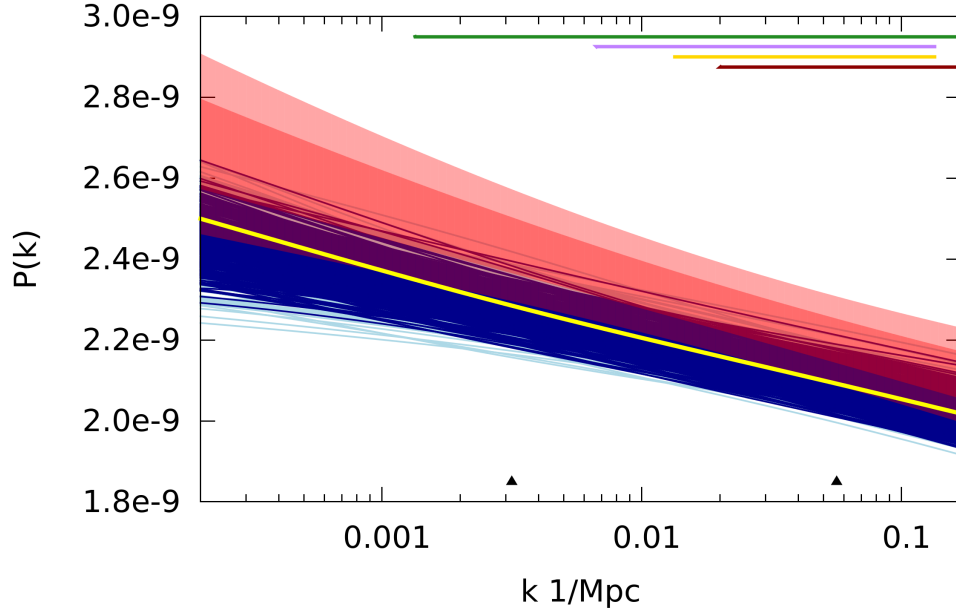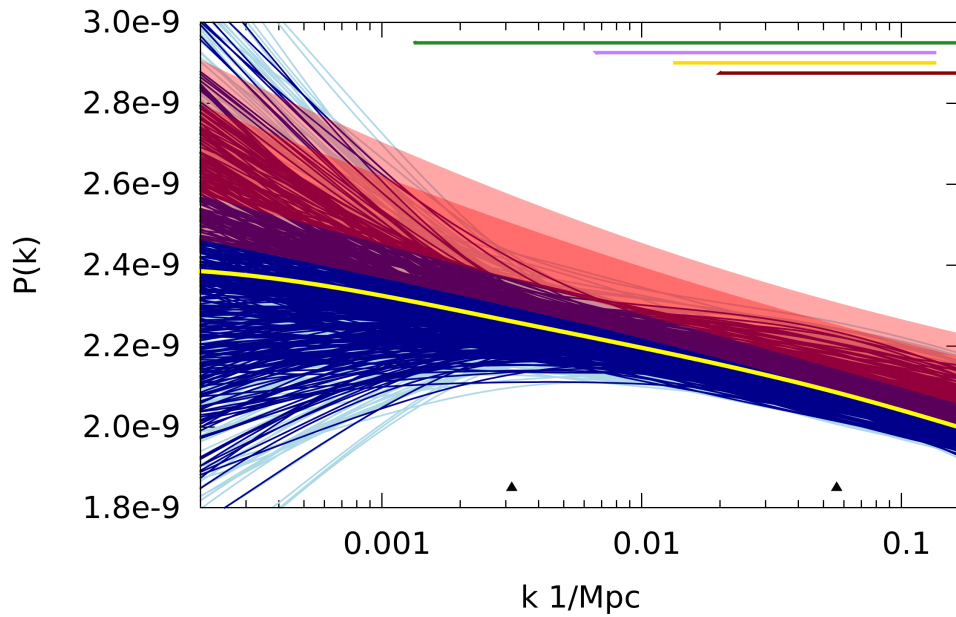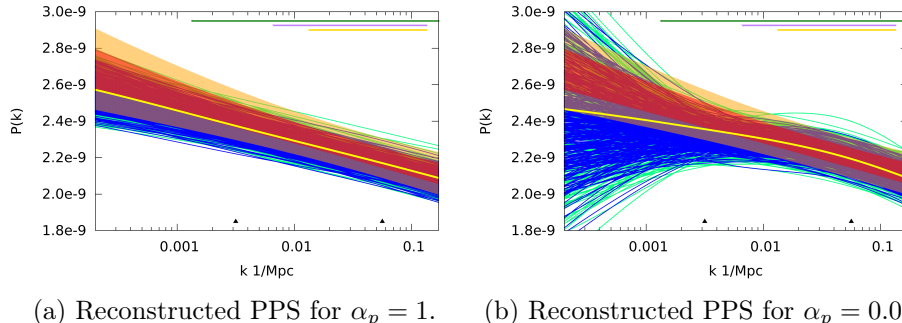
(a) Reconstructed PPS for the final run with $\alpha_p = 1$.

(b) Reconstructed PPS for the final run with $\alpha_p = 0.01$.

Figure 6.3: The splines with the best fit parameters are in yellow. Errors are shown by plotting in dark blue (light blue) 400 spline picked at random among the 68.27% most likely points (points in the range 68.27% - 95.45%) in the MCMC. The red (pale red) region shows the $\pm 1\sigma$ ($\pm 2\sigma$) contour for *Planck* TT, TE, EE + Low P. The black triangles on the bottom show the positions of the knots (some are not visible on the shown scales). The coloured lines on the upper side show the scales probed by each experiment as in figure 5.4, green for *Planck* lensing, lilac for WiggleZ, gold for SDSS DR7, burgundy for CFHTLenS. *Planck* CMB temperature spectrum covers the whole plot.

(a) Reconstructed PPS for $\alpha_p = 1$.   (b) Reconstructed PPS for $\alpha_p = 0.01$.

Figure 6.4: Reconstructed PPS for a run with CMB + *Planck* Lensing + WiggleZ + SDSS DR7. For details on the colour code cf figure 6.3 caption.

oscillations and no modulations due to a step or other models among those in chapter 3.

Despite the errors being comparable with errors from Planck, the results do not match perfectly. Our best fit is 2σ away from *Planck* best fit. The reason could be in a trade off in the value of τ_{reio} and the normalization of the power spectrum. It will be interesting to repeat the analysis fixing that parameter to the best fit from *Planck* to see how the results change. A second possibility comes from unexplored tension between the datasets we used.

Keeping in mind that there might be some incongruence in the data, we can look again at the cross-validation scores in figure 5.5 and 5.6. The CV score of the run 1.2, which confronts WiggleZ with CFHTLenS, has a slightly different behaviour than the other CV scores. In fact at high penalty the CV score does not increase in a very sharp way, and its minimum is placed at a rather high $\alpha_p = 10$. Of course those are not facts that alone have statistical significance. If they had we would have discussed them a priori and not a posteriori, like we are doing. But we can take them as just an hint that the tension is due to CFHTLenS. Those considerations might justify our guess about CFHTLenS being the source of the tension, but are by no mean a proof of tension. More importantly, in section 5.1 we already cited the known tension between CFHTLenS and *Planck* data on σ_8 determination, and we provided references of studies that discuss about it.

To further investigate the tension between the datasets we repeated the analysis omitting CFHTLenS. For lack of computational time we used *Planck* 2013 data release and not *Planck* 2015 data release in this run. We are positive that this will not make a big difference because *Planck* best fit of 2013 data and of 2015 data are completely compatible [23, 1]. As we show in figure 6.4a and 6.4b, removing this dataset does increase the compatibility between our reconstruction and *Planck* best fit power law. However the shape is not affected by the removal as much as the normalization of the PPS.

Further studies about the implication of CFHTLenS on the reconstructed PPS

amplitude should be carried on.

As the main discordance with *Planck* power law PPS seems to be the normalization, we find useful to show the results in another form. If we call our reconstructed PPS, which we know slightly differ from a power law, $\mathcal{P}(k)$, we can still parametrize it in the form

$$\mathcal{P}(k) = A \left(\frac{k}{k_0} \right)^{n(k)-1}, \tag{6.1}$$

just by requiring that the exponent n is a function of the scale. Solving for $n(k)$ we obtain

$$n(k) = \frac{\log[\mathcal{P}(k)] - \log(A)}{\log(k) - \log(k_0)} + 1. \tag{6.2}$$

A plot of this quantity is less sensitive to variations of A as they are logarithmically suppressed. Such a plot is presented in figure 6.5a for $\alpha_p = 1$ and in 6.5b for $\alpha_p = 0.01$.

Again, our more conservative result has errors comparable with Planck.

As we expected the reparametrization shows that the scale dependence of the reconstructed PPS and of the *Planck* PPS are indeed compatible. This proves that the problem is in the normalization of the amplitude and not in the shape itself.

Another one of the main points of our results is that we strongly disprove scale invariance. For both the more conservative and the more free reconstructions, not even one point of the more than 120.000-points-sized MCMC falls near scale invariance. For the very same reason, i.e. the absence of point in that region, we cannot associate a likelihood to scale invariance, and say that we disprove it at a definite confidence level. It would require that the likelihood had been explored even in that highly unlikely region. Our result is remarkable as we have found it in a minimally parametric analysis. So it is independent of whatever inflation model one can choose, and it has value outside of the inflationary paradigm too. Current data do not support scale invariance independently of the model one want to consider whether inflationary, or outside the inflationary paradigm, e.g. cyclic models [52].

Finally we find useful to show a last couple of plots, representing our reconstructed PPS divided k per k by the *Planck* best fit PPS. In figure 6.6a there is the result for $\alpha_p = 1$ and in 6.6b for $\alpha_p = 0.01$.

Of course the two plots are again affected by the discussed difference in the amplitude of our reconstructed PPS and in the amplitude of *Planck* PPS. This explains why the whole set of shown lines (we repeat that every spline has been divided by the *Planck* best fit power law PPS) is well below 1. Despite the amplitude issue, not even one spline reconstruct the shape expected for a damping due to neutrino with sum of the masses equal to 0.4 eV, constraint proposed in [27]. To visualize it in the figure we show in shades of red the damping due to
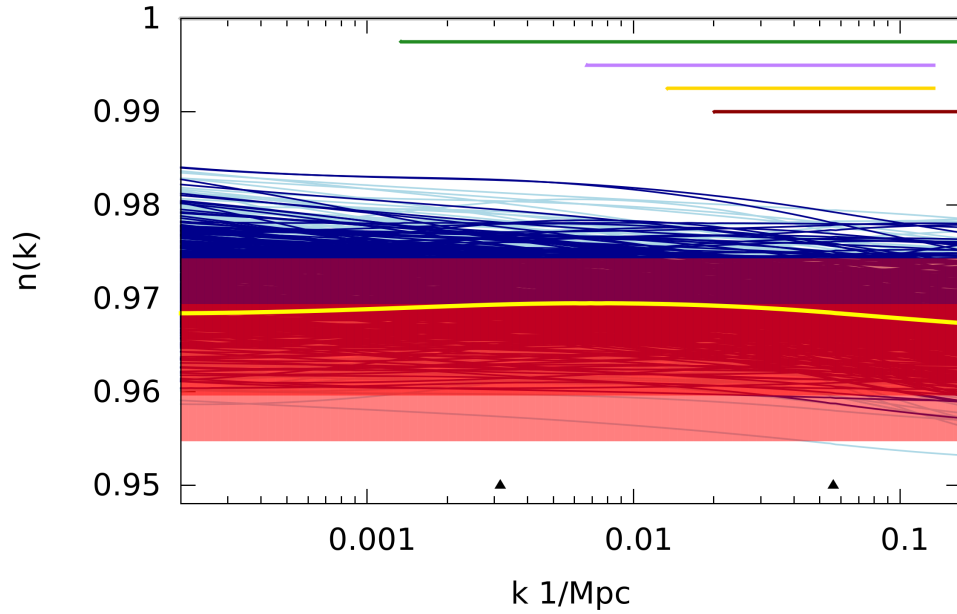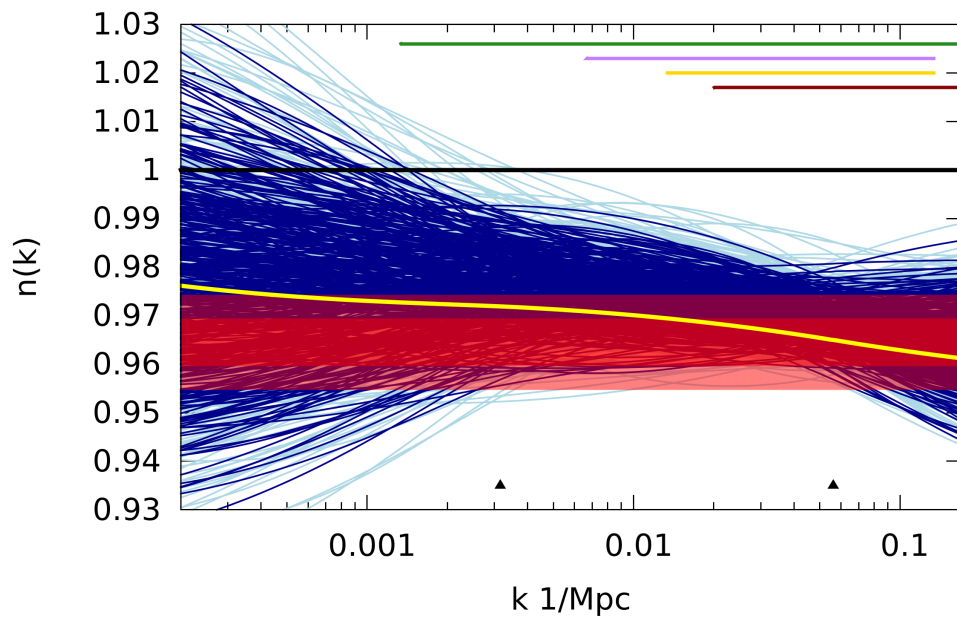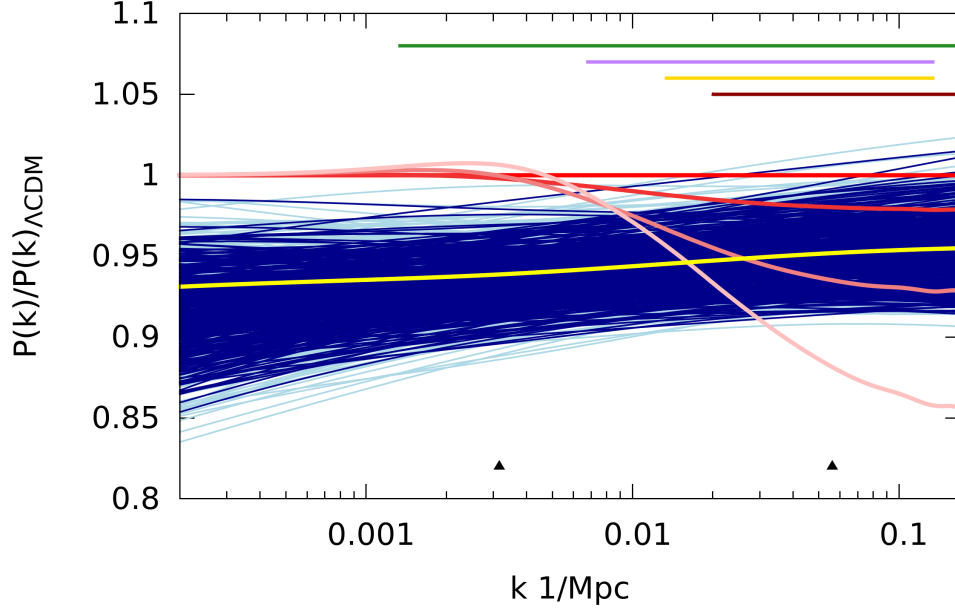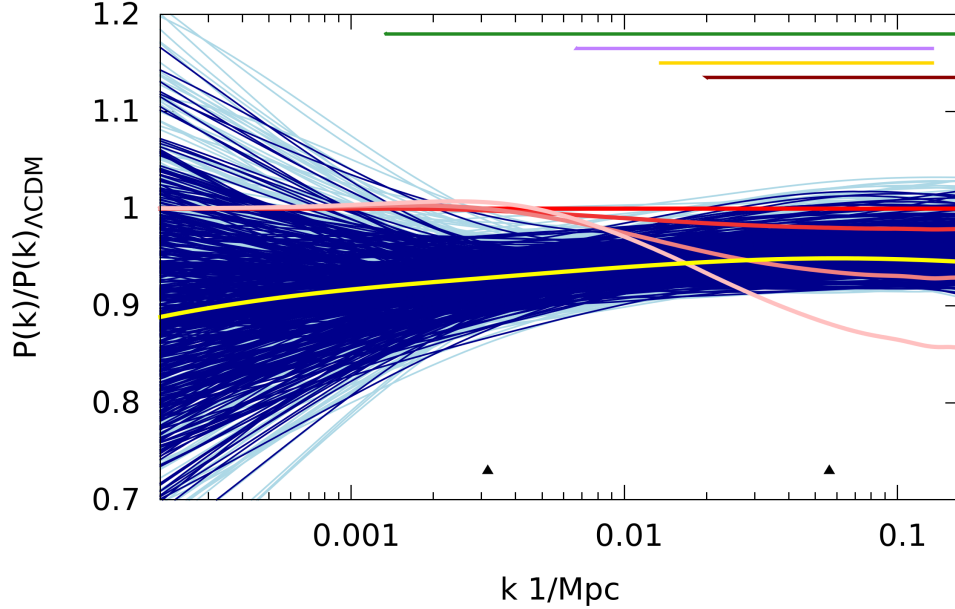
(a) Reconstructed PPS for the final run with $\alpha_p = 1$.

(b) Reconstructed PPS for the final run with $\alpha_p = 0.01$.

Figure 6.5: The splines with the best fit parameters are in yellow. Errors are shown by plotting in dark blue (light blue) 400 spline picked at random among the 68.27% most likely points (points in the range 68.27% - 95.45%) in the MCMC. The red (pale red) region shows the $\pm 1\sigma$ ($\pm 2\sigma$) contour for *Planck* TT, TE, EE + Low P. The black triangles on the bottom show the positions of the knots (some are not visible on the shown scales). The coloured lines on the upper side show the scales probed by each experiment as in figure 5.4, green for *Planck* lensing, lilac for WiggleZ, gold for SDSS DR7, burgundy for CFHTLenS. *Planck* CMB temperature spectrum covers the whole plot. In the bottom figure, the black line shows $n(k) \equiv 1$, i.e. scale invariance.

(a) Reconstructed PPS for the final run with $\alpha_p = 1$ divided by the *Planck* power law PPS.

(b) Reconstructed PPS for the final run with $\alpha_p = 0.01$ divided by the *Planck* power law PPS.

Figure 6.6: The splines with the best fit parameters are in yellow. Errors are shown by plotting in dark blue (light blue) 400 spline picked at random among the 68.27% most likely points (points in the range 68.27% - 95.45%) in the MCMC. The black triangles on the bottom show the positions of the knots (some are not visible on the shown scales). The coloured lines on the upper side show the scales probed by each experiment as in figure 5.4, green for *Planck* lensing, lilac for WiggleZ, gold for SDSS DR7, burgundy for CFHTLenS. *Planck* CMB temperature spectrum covers the whole plot. In shades of red, we plot damping due to massive neutrinos. From the uppermost to the lowermost is $\Sigma m_\nu =$0 eV, 0.06 eV, 0.2 eV, 0.4 eV.

massive neutrinos. From the uppermost to the lowermost is Σm_ν =0 eV, 0.06 eV, 0.2 eV, 0.4 eV. In our analysis we did not considered the errors on the spline approximation of the PPS shape reported in table 5.1. In fact they are negligible compared to the uncertainties of the fit shown in figure.

We are eager to point out that what we are excluding is not a sum of the masses of neutrinos greater than 0.4 eV alone, but a ΛCDM model plus a sum of the masses of neutrinos equal to 0.4 eV. This is because if the PPS deviates from a power law, enhancing power on small scales, it could cancel with the damping effect of the neutrino masses. But still we are positive that a power law PPS plus a sum of the masses of neutrinos equal or grater than 0.4 eV could be excluded at more than 95% C.L.

Chapter 7

Conclusions

In the present work we reconstructed the primordial power spectrum using a minimally parametric technique. We used a 5 knots cubic spline to parametrize the shape of the PPS. The knots were placed equally spaced in $\log k$ and their positions have been held fixed through all the analysis. Instead the amplitude of the spline on the 5 knots and the cosmological parameters ω_b, ω_{cdm}, h, and τ_{reio} were the free parameters in our fit procedure. To prevent over-fitting data we added in the fit a penalty on the roughness of the spline, and we used cross-validation to optimise the weight of the penalty. We did the fit using the Boltzmann code CLASS and its ancillary Monte Carlo wrapper Monte Python. Those allow to find the best fit value for the parameters using a Markov Chain Monte Carlo in parameter space. The experiments used in the analysis are *Planck*, WMAP, WiggleZ, CFHTLenS, and SDSS DR7. We tried to incorporate in our work all the most recent experiments that could give constraints on the shape of the PPS.

The primary goal of this work has been the setup of the machinery needed for the reconstruction. We have used it with a small amount of knots to fully test it, and we are sure that it is now ready to be used in the near future, without any further modification or additional check. Now that we are well aware of what are its capabilities, and flaws, we can start a "bigger scale" analysis involving more knots and different datasets; such an analysis could not have been took too light heartedly in the beginning because of the required computational time. Using more knots we might be able to further investigate PPS features.

However we want to remark the versatility of the method, that even in the minimal configuration used here has proved to be useful, since it produced many important physical results.

The reconstructed PPS overall amplitude is quite compatible with *Planck* best fit, and the overall tilt is completely compatible with *Planck*. Removing the CFHTLenS datasets from the analysis has a clear effect, as the PPS reconstructed without it has a bigger overall amplitude and a better compatibility with *Planck*. This is probably the outcome of a known tension between *Planck* and CFHTLenS

data.

The reconstruction carries no evidence of any feature. Although it has no statistical significance we notice a small damp at small k that we believe is due to the low multipole "anomaly" of the CMB power spectrum.

We disprove a ΛCDM with a sum of neutrino masses equal or greater than 0.4 eV, as it is so unlikely that not even one point of our MCMC predicts this scenario.

There are two main topics that we think are worth further analysis. The first is to analyse the effect of CFHTLenS on the amplitude of the reconstructed PPS. The second is to try to optimise the positions of the knots, and add a few more. In this way it might be possible to improve the precision of our result.

Chapter 8

Acknowledgements

Bibliography

[1] Planck Collaboration et al. "Planck 2015 results. XIII. Cosmological parameters". In: *ArXiv e-prints* (Feb. 2015). arXiv: `1502.01589` (cit. on pp. 6, 7, 18, 53, 55).

[2] G. Hinshaw et al. "Nine-year Wilkinson Microwave Anisotropy Probe (WMAP) Observations: Cosmological Parameter Results". In: *The Astrophysical Journal Supplement* 208, 19 (Oct. 2013), p. 19. DOI: `10.1088/0067-0049/208/2/19`. arXiv: `1212.5226` (cit. on p. 6).

[3] B. A. Reid et al. "Cosmological constraints from the clustering of the Sloan Digital Sky Survey DR7 luminous red galaxies". In: *Monthly Notices of the Royal Astronomical Society* 404 (May 2010), pp. 60–85. DOI: `10.1111/j.1365-2966.2010.16276.x`. arXiv: `0907.1659 [astro-ph.CO]` (cit. on pp. 6, 44, 49).

[4] David H. Lyth and Andrew R. Liddle. *The Primordial Density Perturbation*. Cambridge university press, 2009 (cit. on pp. 9, 16, 49).

[5] N. Bartolo et al. "Non-Gaussianity from inflation: theory and observations". In: *Physics Reports* 402 (Nov. 2004), pp. 103–266. DOI: `10.1016/j.physrep.2004.08.022`. eprint: `astro-ph/0406398` (cit. on pp. 9, 11, 12, 14, 17).

[6] Hideo Kodama and Misao Sasaki. "Cosmological Perturbation Theory". In: *Progress of Theoretical Physics Supplement* 78 (1984), pp. 1–166. DOI: `10.1143/PTPS.78.1`. eprint: `http://ptps.oxfordjournals.org/content/78/1.full.pdf+html`. URL: `http://ptps.oxfordjournals.org/content/78/1.abstract` (cit. on p. 17).

[7] K. A. Malik and D. Wands. "Cosmological perturbations". In: *Physics Reports* 475 (May 2009), pp. 1–51. DOI: `10.1016/j.physrep.2009.03.001`. arXiv: `0809.4944` (cit. on pp. 17, 35).

[8] Planck Collaboration et al. "Planck 2015 results. XX. Constraints on inflation". In: *ArXiv e-prints* (Feb. 2015). arXiv: `1502.02114` (cit. on pp. 18–21, 33).

[9] V. Miranda and W. Hu. "Inflationary steps in the Planck data". In: *Physical Review D* 89.8, 083529 (Apr. 2014), p. 083529. DOI: `10.1103/PhysRevD.89.083529`. arXiv: `1312.0946` (cit. on p. 19).

[10] P. D. Meerburg, D. N. Spergel, and B. D. Wandelt. "Searching for oscillations in the primordial power spectrum. II. Constraints from Planck data". In: *Physical Review D* 89.6, 063537 (Mar. 2014), p. 063537. DOI: 10.1103/PhysRevD.89.063537. arXiv: 1308.3705 (cit. on pp. 21, 22).

[11] X. Chen, M. H. Namjoo, and Y. Wang. "Models of the Primordial Standard Clock". In: *Journal of Cosmology and Astroparticle Physics* 2, 027 (Feb. 2015), p. 27. DOI: 10.1088/1475-7516/2015/02/027. arXiv: 1411.2349 (cit. on p. 21).

[12] U. H. Danielsson. "Note on inflation and trans-Planckian physics". In: *Physical Review D* 66.2, 023511 (July 2002), p. 023511. DOI: 10.1103/PhysRevD.66.023511. eprint: hep-th/0203198 (cit. on p. 22).

[13] C. Sealfon, L. Verde, and R. Jimenez. "Smoothing spline primordial power spectrum reconstruction". In: *Physical Review D* 72.10, 103520 (Nov. 2005), p. 103520. DOI: 10.1103/PhysRevD.72.103520. eprint: astro-ph/0506707 (cit. on pp. 23, 24, 29).

[14] Carl de Boor. *A Practical Guide to Splines*. Springer-Verlag, 1978 (cit. on pp. 24, 32).

[15] R. Trotta. "Bayes in the sky: Bayesian inference and model selection in cosmology". In: *Contemporary Physics* 49 (Mar. 2008), pp. 71–104. DOI: 10.1080/00107510802066753. arXiv: 0803.4089 (cit. on p. 26).

[16] L. Verde. "A practical guide to Basic Statistical Techniques for Data Analysis in Cosmology". In: *ArXiv e-prints* (Dec. 2007). arXiv: 0712.3028 (cit. on p. 26).

[17] Nelson Christensen and Renate Meyer. "Using Markov chain Monte Carlo methods for estimating parameters with gravitational radiation data". In: *Physical Review D* 64 (2 May 2001), p. 022001. DOI: 10.1103/PhysRevD.64.022001. URL: http://link.aps.org/doi/10.1103/PhysRevD.64.022001 (cit. on p. 26).

[18] Andrew Gelman and Donald B. Rubin. "Inference from Iterative Simulation Using Multiple Sequences". In: *Statistical Science* 7 (1992) (cit. on p. 27).

[19] P.J. Green and B.W. Silverman. *Nonparametric regression and generalized linear models: a roughness penalty approach*. Chapman & Hall, 1994. ISBN: 0412300400 (cit. on p. 29).

[20] D. Blas, J. Lesgourgues, and T. Tram. "The Cosmic Linear Anisotropy Solving System (CLASS). Part II: Approximation schemes". In: *Journal of Cosmology and Astroparticle Physics* 7, 034 (July 2011), p. 34. DOI: 10.1088/1475-7516/2011/07/034. arXiv: 1104.2933 (cit. on p. 31).

[21] Benjamin Audren et al. "Conservative Constraints on Early Cosmology: an illustration of the Monte Python cosmological parameter inference code". In: *JCAP* 1302 (2013), p. 001. DOI: `10.1088/1475-7516/2013/02/001`. arXiv: `1210.7183 [astro-ph.CO]` (cit. on p. 31).

[22] J. Lesgourgues and S. Pastor. "Massive neutrinos and cosmology". In: *Physics Reports* 429 (July 2006), pp. 307–379. DOI: `10.1016/j.physrep.2006.04.001`. eprint: `astro-ph/0603494` (cit. on pp. 34, 37, 49).

[23] Planck Collaboration et al. "Planck 2013 results. XVI. Cosmological parameters". In: *Astronomy & Astrophysics* 571, A16 (Nov. 2014), A16. DOI: `10.1051/0004-6361/201321591`. arXiv: `1303.5076 [astro-ph.CO]` (cit. on pp. 34, 35, 38, 55).

[24] Adam G. Riess et al. "A 3 percent Solution: Determination of the Hubble Constant with the Hubble Space Telescope and Wide Field Camera 3". In: *The Astrophysical Journal* 730.2 (2011), p. 119. URL: `http://stacks.iop.org/0004-637X/730/i=2/a=119` (cit. on p. 34).

[25] Planck Collaboration et al. "Planck 2013 results. XX. Cosmology from Sunyaev-Zeldovich cluster counts". In: *Astronomy & Astrophysics* 571, A20 (Nov. 2014), A20. DOI: `10.1051/0004-6361/201321521`. arXiv: `1303.5080` (cit. on p. 34).

[26] L. Verde, P. Protopapas, and R. Jimenez. "Planck and the local Universe: Quantifying the tension". In: *Physics of the Dark Universe* 2.3 (2013), pp. 166–175. ISSN: 2212-6864. DOI: `http://dx.doi.org/10.1016/j.dark.2013.09.002`. URL: `http://www.sciencedirect.com/science/article/pii/S2212686413000319` (cit. on p. 35).

[27] Richard A. Battye and Adam Moss. "Evidence for Massive Neutrinos from Cosmic Microwave Background and Lensing Observations". In: *Phys. Rev. Lett.* 112 (5 Feb. 2014), p. 051303. DOI: `10.1103/PhysRevLett.112.051303`. URL: `http://link.aps.org/doi/10.1103/PhysRevLett.112.051303` (cit. on pp. 35, 56).

[28] Mark Wyman et al. "Neutrinos Help Reconcile Planck Measurements with the Local Universe". In: *Phys. Rev. Lett.* 112 (5 Feb. 2014), p. 051302. DOI: `10.1103/PhysRevLett.112.051302`. URL: `http://link.aps.org/doi/10.1103/PhysRevLett.112.051302` (cit. on p. 35).

[29] Jan Hamann and Jasper Hasenkamp. "A new life for sterile neutrinos: resolving inconsistencies using hot dark matter". In: *Journal of Cosmology and Astroparticle Physics* 2013.10 (2013), p. 044. URL: `http://stacks.iop.org/1475-7516/2013/i=10/a=044` (cit. on p. 35).

[30] F. Beutler et al. "The clustering of galaxies in the SDSS-III Baryon Oscil-
      lation Spectroscopic Survey: signs of neutrino mass in current cosmological
      data sets". In: *Monthly Notices of the Royal Astronomical Society* 444 (Nov.
      2014), pp. 3501–3516. DOI: `10.1093/mnras/stu1702`. arXiv: `1403.4599`
      (cit. on p. 35).

[31] E. Giusarma et al. "Relic neutrinos, thermal axions, and cosmology in early
      2014". In: *Physical Review D* 90.4, 043507 (Aug. 2014), p. 043507. DOI:
      `10.1103/PhysRevD.90.043507`. arXiv: `1403.4852` (cit. on p. 35).

[32] P. A. R. Ade et al. "Detection of B-Mode Polarization at Degree Angular
      Scales by BICEP2". In: *Phys. Rev. Lett.* 112 (24 June 2014), p. 241101. DOI:
      `10.1103/PhysRevLett.112.241101`. URL: `http://link.aps.org/doi/10.`
      `1103/PhysRevLett.112.241101` (cit. on p. 35).

[33] Stephen M. Feeney, Hiranya V. Peiris, and Licia Verde. "Is there evidence
      for additional neutrino species from cosmology?" In: *Journal of Cosmology
      and Astroparticle Physics* 2013.04 (2013), p. 036. URL: `http://stacks.`
      `iop.org/1475-7516/2013/i=04/a=036` (cit. on p. 35).

[34] Jian-Wei Hu et al. "Cosmological parameter estimation from CMB and X-
      ray cluster after Planck". In: *Journal of Cosmology and Astroparticle Physics*
      2014.05 (2014), p. 020. URL: `http://stacks.iop.org/1475-7516/2014/`
      `i=05/a=020` (cit. on p. 35).

[35] Licia Verde et al. "(Lack of) Cosmological evidence for dark radiation after
      Planck". In: *Journal of Cosmology and Astroparticle Physics* 2013.09 (2013),
      p. 013. URL: `http://stacks.iop.org/1475-7516/2013/i=09/a=013` (cit.
      on p. 35).

[36] G. Efstathiou. "H_0 revisited". In: *Monthly Notices of the Royal Astronomical
      Society* 440 (May 2014), pp. 1138–1152. DOI: `10.1093/mnras/stu278`.
      arXiv: `1311.3461` (cit. on p. 35).

[37] B. Leistedt, H. V. Peiris, and L. Verde. "No New Cosmological Concordance
      with Massive Sterile Neutrinos". In: *Physical Review Letters* 113.4, 041301
      (July 2014), p. 041301. DOI: `10.1103/PhysRevLett.113.041301`. arXiv:
      `1404.5950` (cit. on p. 35).

[38] Silvia Pascoli and Thomas Schwetz. "Prospects for Neutrino Oscillation
      Physics". In: *Advances in High Energy Physics* 2013 (2013), pp. 1–29. DOI:
      `10.1155/2013/503401`. URL: `http://dx.doi.org/10.1155/2013/503401`
      (cit. on p. 38).

[39] Scott Dodelson. *Modern Cosmology*. Academic Press, 2003. ISBN: 1852337613
      (cit. on pp. 38, 43, 49).

[40] Planck Collaboration et al. "Planck 2013 results. I. Overview of products
      and scientific results". In: *Astronomy & Astrophysics* 571, A1 (Nov. 2014),
      A1. DOI: `10.1051/0004-6361/201321529`. arXiv: `1303.5062` (cit. on p. 42).

[41] Planck Collaboration et al. "Planck 2013 results. XV. CMB power spectra and likelihood". In: *Astronomy & Astrophysics* 571, A15 (Nov. 2014), A15. DOI: `10.1051/0004-6361/201321573`. arXiv: `1303.5075` (cit. on pp. 43, 53).

[42] C. L. Bennett et al. "Nine-year Wilkinson Microwave Anisotropy Probe (WMAP) Observations: Final Maps and Results". In: *The Astrophysical Journal Supplement* 208, 20 (Oct. 2013), p. 20. DOI: `10.1088/0067-0049/208/2/20`. arXiv: `1212.5225 [astro-ph.CO]` (cit. on p. 43).

[43] Planck Collaboration et al. "Planck 2013 results. XVII. Gravitational lensing by large-scale structure". In: *Astronomy & Astrophysics* 571, A17 (Nov. 2014), A17. DOI: `10.1051/0004-6361/201321543`. arXiv: `1303.5077` (cit. on p. 43).

[44] C. Heymans et al. "CFHTLenS: the Canada-France-Hawaii Telescope Lensing Survey". In: *Monthly Notices of the Royal Astronomical Society* 427 (Nov. 2012), pp. 146–166. DOI: `10.1111/j.1365-2966.2012.21952.x`. arXiv: `1210.0032 [astro-ph.CO]` (cit. on pp. 44, 49).

[45] T. Erben et al. "CFHTLenS: the Canada-France-Hawaii Telescope Lensing Survey - imaging data and catalogue products". In: *Monthly Notices of the Royal Astronomical Society* 433 (Aug. 2013), pp. 2545–2563. DOI: `10.1093/mnras/stt928`. arXiv: `1210.8156 [astro-ph.CO]` (cit. on p. 44).

[46] L. Miller et al. "Bayesian galaxy shape measurement for weak lensing surveys - III. Application to the Canada-France-Hawaii Telescope Lensing Survey". In: *Monthly Notices of the Royal Astronomical Society* 429 (Mar. 2013), pp. 2858–2880. DOI: `10.1093/mnras/sts454`. arXiv: `1210.8201 [astro-ph.CO]` (cit. on p. 44).

[47] H. Hildebrandt et al. "CFHTLenS: improving the quality of photometric redshifts with precision photometry". In: *Monthly Notices of the Royal Astronomical Society* 421 (Apr. 2012), pp. 2355–2367. DOI: `10.1111/j.1365-2966.2012.20468.x`. arXiv: `1111.4434 [astro-ph.CO]` (cit. on p. 44).

[48] C. Heymans et al. "The impact of high spatial frequency atmospheric distortions on weak-lensing measurements". In: *Monthly Notices of the Royal Astronomical Society* 421 (Mar. 2012), pp. 381–389. DOI: `10.1111/j.1365-2966.2011.20312.x`. arXiv: `1110.4913 [astro-ph.CO]` (cit. on p. 44).

[49] J. Benjamin et al. "CFHTLenS tomographic weak lensing: quantifying accurate redshift distributions". In: *Monthly Notices of the Royal Astronomical Society* 431 (May 2013), pp. 1547–1564. DOI: `10.1093/mnras/stt276`. arXiv: `1212.3327 [astro-ph.CO]` (cit. on p. 44).

[50]   D. Parkinson et al. "The WiggleZ Dark Energy Survey: Final data re-
        lease and cosmological results". In: *Physical Review D* 86.10, 103518 (Nov.
        2012), p. 103518. DOI: `10.1103/PhysRevD.86.103518`. arXiv: `1210.2130`
        `[astro-ph.CO]` (cit. on pp. 44, 49).

[51]   Planck Collaboration et al. "Planck 2015 results. XI. CMB power spectra,
        likelihoods, and robustness of parameters". In: *ArXiv e-prints* (July 2015).
        arXiv: `1507.02704` (cit. on p. 49).

[52]   P. J. Steinhardt and N. Turok. "Cosmic evolution in a cyclic universe". In:
        Physical Review D 65.12, 126003 (June 2002), p. 126003. DOI: `10.1103/`
        `PhysRevD.65.126003`. eprint: `hep-th/0111098` (cit. on p. 56).